

1-1-2005

# Piezo drive tunable optic filter

Wen Zu  
*Ryerson University*

Follow this and additional works at: <http://digitalcommons.ryerson.ca/dissertations>



Part of the [Electrical and Computer Engineering Commons](#)

---

## Recommended Citation

Zu, Wen, "Piezo drive tunable optic filter" (2005). *Theses and dissertations*. Paper 416.

This Thesis is brought to you for free and open access by Digital Commons @ Ryerson. It has been accepted for inclusion in Theses and dissertations by an authorized administrator of Digital Commons @ Ryerson. For more information, please contact [bcameron@ryerson.ca](mailto:bcameron@ryerson.ca).

## **NOTE TO USERS**

**This reproduction is the best copy available.**

UMI<sup>®</sup>



# PIEZO DRIVE TUNABLE OPTIC FILTER

by

WEN ZU

B.Eng., North China Institute of Technology  
China, 1990

A thesis

presented to Ryerson University

in partial fulfillment of the  
requirement for the degree of  
Master of Applied Science  
in the Program of  
Electrical and Computer Engineering

Toronto, Ontario, Canada, 2005

©WEN ZU 2005

PROPERTY OF  
RYERSON UNIVERSITY LIBRARY

UMI Number: EC53792

#### INFORMATION TO USERS

The quality of this reproduction is dependent upon the quality of the copy submitted. Broken or indistinct print, colored or poor quality illustrations and photographs, print bleed-through, substandard margins, and improper alignment can adversely affect reproduction.

In the unlikely event that the author did not send a complete manuscript and there are missing pages, these will be noted. Also, if unauthorized copyright material had to be removed, a note will indicate the deletion.

UMI<sup>®</sup>

---

UMI Microform EC53792  
Copyright 2009 by ProQuest LLC  
All rights reserved. This microform edition is protected against  
unauthorized copying under Title 17, United States Code.

---

ProQuest LLC  
789 East Eisenhower Parkway  
P.O. Box 1346  
Ann Arbor, MI 48106-1346

## Author's Declaration

I hereby declare that I am the sole author of this thesis.

I authorize Ryerson University to lend this thesis to other institutions or individuals for the purpose of scholarly research.

(Wen Zu)

---

I further authorize Ryerson University to reproduce this thesis by photocopying or by other means, in total or in part, at the request of other institutions or individuals for the purpose of scholarly research.

(Wen Zu)

---

## Borrower's Page

Ryerson University requires the signatures of all persons using or photocopying this thesis. Please sign below, and give address and date.

[illegible]

# **ABSTRACT**

## **Piezo Drive Tunable Optic Filter**

**©Wen Zu 2005**

**Master of Applied Science  
Department of Electrical and Computer Engineering  
Ryerson University**

Tunable fiber optic filter has extensive applications in telecommunication, spectroscopy, and fiber optic sensing. Many research attempts have been devoted to develop a filter with a wide tuning range, a fast tuning speed, a fine tuning resolution, and high reliability. Despite of the progress made so far, a tunable fiber optic filter that combines all these qualities is still a subject of intensive research.

This thesis describes the design, fabrication and test results of a high performance tunable fiber optic filter. The filter is piezo-driven using a flexural hinge structure for displacement magnification and an axial strain of a fiber Bragg grating. Finite element analysis was used to design the mechanical structure to achieve the required displacement magnification and reaction force for grating compression. A passive thermal compensation design was implemented with two spacers of different coefficients of thermal expansion to compensate the thermal-induced wavelength drift. A feedback control system with a linear variable differential transformer was employed to control the displacement and to achieve the designed tuning accuracy.

A tuning range of 13.7 nm, a maximum closed loop switching time of 17.3 ms, and a wavelength drift of 1.4 pm/C were achieved. The flexural-hinge structure, that offers noise-free motion, no need of lubricants and no wear, ensures its long-term reliability.



## Acknowledgement

I would like to thank my supervisor Dr. X. J. Gu for his continuous guidance and encouragement through the course of my research work. I would also like to thank Mr. Jinmin He, Dr. Y. Xu and Mr. Yifeng He for their enlightening comments and suggestions. This work would have been impossible without their feedback, patience and kindness.

I would also like to thank the Department of Electrical and Computer Engineering for providing a very well equipped and technically supported Ryerson Optic Sensing and Communication Laboratory. My thanks are due to the School of Graduate Studies of Ryerson University for providing Graduate Student Scholarship.

I would like to acknowledge my supervisor's funding resource, the Discovery Grant from the National Science and Engineering Research Council of Canada, for providing me financial support throughout my research work.

In the end, I would like to say thanks to my wife and my sons. I could not have achieved this goal without their love, tolerance, encouragement and support.

# Contents

<b>1</b>	<b>Introduction</b>	<b>1</b>
1.1	Review of Tunable Filter Technologies . . . . .	1
1.2	Review of FBG-based Filters . . . . .	3
1.3	Motivations . . . . .	5
1.4	Outline of Thesis . . . . .	6
<b>2</b>	<b>Filter Design and Fabrication</b>	<b>8</b>
2.1	Introduction . . . . .	8
2.2	Piezo Element . . . . .	9
2.3	Mechanical designs . . . . .	10
2.3.1	Design Requirement . . . . .	10
2.3.2	Finite Element Analysis of Actuator . . . . .	12
2.3.3	Mechanical Design of Actuator . . . . .	18
2.3.4	Mechanical Design of FBG guiding . . . . .	18
2.4	Thermal Compensation Design . . . . .	20
2.4.1	Introduction . . . . .	20
2.4.2	Actuator Thermal Effect Analysis . . . . .	21
2.4.3	Spacers Calculation and Design . . . . .	23
2.5	Electronic Designs . . . . .	25
2.5.1	LVDT Driver Circuit Design . . . . .	26
2.5.2	Subtractor Amplifier Design . . . . .	31
2.5.3	Low Noise DC Power Supply Circuit Design . . . . .	32
2.5.4	PCB Design . . . . .	33
2.6	Labview Programming . . . . .	34
2.7	Filter Fabrication . . . . .	38
2.7.1	Parts Machining . . . . .	38
2.7.2	PCB Assembly . . . . .	38
2.7.3	FBG Guiding . . . . .	39
2.7.4	Filter Assembly . . . . .	40
<b>3</b>	<b>Filter Tests and Measurements</b>	<b>41</b>
3.1	Introduction . . . . .	41
3.2	Tests Setup . . . . .	42
3.2.1	Optic Test Setup . . . . .	42
3.2.2	Instruments and Components Used In Tests . . . . .	43

3.3	Tunable Filter Calibration . . . . .	43
3.4	Closed Loop Tuning Speed/Switching Time . . . . .	45
3.5	Short and Long Term Drift . . . . .	48
3.6	Wavelength tuning Repeatability . . . . .	49
3.7	Tuning Resolution . . . . .	51
3.8	Thermal Compensation Test . . . . .	53
3.9	Filter Applications Test . . . . .	54
<b>4</b>	<b>Conclusions</b>	<b>57</b>
4.1	Summary of thesis . . . . .	57
4.2	Contributions . . . . .	58
4.3	Future research . . . . .	59
4.3.1	Displacement Expanders with Large Stroke Gain Under a Force Load . . . . .	59
4.3.2	Rebuild ANSYS Model For Thermal Compensation Calculation	63
4.3.3	Improve The AD698's Heat Dissipation . . . . .	64
4.3.4	Re-design The Fiber Guiding System . . . . .	64
4.3.5	Expand The Application of The Tunable Filter . . . . .	64
	<b>Bibliography</b>	<b>65</b>
	<b>A Drawings of Mechanical Design</b>	<b>70</b>
	<b>B Drawings of PCB</b>	<b>74</b>
	<b>C Ansys Command Log</b>	<b>77</b>

# List of Figures

1.1	Scheme of writing a FBG . . . . .	4
1.2	FBG Core . . . . .	4
2.1	Schematic of a PZT Single Layer Structure . . . . .	9
2.2	Stroke/Voltage Diagram of Piezo Stack . . . . .	10
2.3	Guided FBG . . . . .	11
2.4	Half actuator with 8 flexural-hinges . . . . .	13
2.5	3-D actuator . . . . .	14
2.6	Model of actuator after meshing . . . . .	14
2.7	Boundary Condition . . . . .	15
2.8	Structure deformation under $U_x = 25\mu m$ . . . . .	16
2.9	Actuator . . . . .	18
2.10	Accessorial parts of the actuator . . . . .	19
2.11	Thermal compensation structure . . . . .	20
2.12	ANSYS result of the thermal effect on the actuator . . . . .	21
2.13	Frame without flexible hinges . . . . .	22
2.14	Actuator thermal effect calculation . . . . .	23
2.15	Thermal expansion of spacers and piezo stacks (x-direction) . . . . .	25
2.16	Electronic block diagram of the tunable filter . . . . .	26
2.17	LVDT . . . . .	26
2.18	LVDT driven by a signal conditioner . . . . .	27
2.19	LVDT driven by AD698 . . . . .	28
2.20	Excitation voltage $V_{EXC}$ vs. R1 . . . . .	30
2.21	Output voltage ripple vs. Filter Capacitance . . . . .	31
2.22	+5V Reference . . . . .	31
2.23	Subtractor . . . . .	32
2.24	DC Power Supply for Subtractor . . . . .	33
2.25	PCB Layout . . . . .	34
2.26	Labview diagram for the 20Hz control signal generator . . . . .	35
2.27	Labview diagram for the pulse signal generator . . . . .	35
2.28	Labview diagram for the repeatability test . . . . .	36
2.29	Labview diagram for the wavelength tuning . . . . .	36
2.30	Labview diagram for reading LVDT . . . . .	37
2.31	FBG Guiding . . . . .	39
2.32	Filter assembly . . . . .	40

3.1	Optic system setup A . . . . .	42
3.2	Optic system setup B . . . . .	42
3.3	Filter Calibration (LVDT vs. Wavelength) . . . . .	44
3.4	Control signal vs. Photo detector . . . . .	46
3.5	Control signal vs. LVDT output . . . . .	47
3.6	Switching time variation . . . . .	48
3.7	Short term drift . . . . .	48
3.8	Long term drift . . . . .	49
3.9	Tuning repeatability of the filter tuned 20 times to three different wave- lengths . . . . .	50
3.10	The corresponding LVDT measurements when the filter were tuned to three different wavelengths for 20 times . . . . .	50
3.11	Resolution of the filter . . . . .	51
3.12	Corresponding output of the LVDT . . . . .	52
3.13	Result of the thermal test, Case V . . . . .	54
3.14	(a)The Spectra of Thin Film Filter measured by the tunable filter (b)Filter measured by an OSA . . . . .	55
3.15	FBG Reflection Spectra . . . . .	56
4.1	Double-Ti-Hinge Actuator . . . . .	62
4.2	Single-Ti-Hinge Actuator . . . . .	62
A.1	Actuator . . . . .	70
A.2	Upper Holder . . . . .	71
A.3	Lower Holder . . . . .	71
A.4	Sleeve . . . . .	72
A.5	LVDT Holder . . . . .	72
A.6	Spacer A . . . . .	73
A.7	Spacer B . . . . .	73
B.1	Top Layer . . . . .	74
B.2	Bottom Layer . . . . .	75
B.3	Top-Over Layer . . . . .	75
B.4	Drill . . . . .	76

# List of Tables

1.1	A Comparison of FBG-based optic tunable filters from three references	6
1.2	Characteristics of the tunable filter . . . . .	6
2.1	Material properties . . . . .	12
2.2	Structure deformation . . . . .	16
2.3	Hinge optimization . . . . .	17
2.4	Force vs. Deformation . . . . .	17
3.1	Instruments and devices . . . . .	43
3.2	Filter calibration . . . . .	45
3.3	The results of thermal tests with different spacers . . . . .	53
4.1	Characteristics of the tunable filter . . . . .	58
4.2	Filter made of the annealed hot rolled Invar 36 vs. Filter made of the cold drawn Invar 36 . . . . .	60
4.3	A comparison of material properties . . . . .	61

# Chapter 1

## Introduction

### 1.1 Review of Tunable Filter Technologies

**O**PTICAL networks have been a reality as the physical layer of high-performance telecommunication networks. The tunable filter grows in the applications to optic performance monitoring, tunable laser, optical add drop multiplexing (OADM), wavelength-division multiplexing (WDM), tunable receivers, tunable external cavity laser(ECL),and dispersion compensation.

There are a number of different tunable filter constructions with different tuning techniques, including angle-tuned interference filter (ATIF), waveguided Mach-Zehnder filter (MZF), Fabry-Perot etalon filter (FPF), acoustic optic tunable filter (AOTF), diffraction grating filter (DGF), tunable spectral slicing filter (TSSF), micro-electro-mechanical system (MEMS) filter, and fiber Bragg grating (FBG)filter.

ATIFs, otherwise known as thin film filters, were the first multi-wavelength type of filters to be used in WDM. They are made by depositing a series of thin layers of coatings of two materials with different refractive indexes. ATIFs can be made tunable by changing the angle of incident light. This kind of filters has a sufficiently low crosstalk and a narrow bandwidth [1], in addition to the lower cost since they can be mass-produced.

MZFs are based on the difference in length between two sources that interfere with each other. The length difference introduces a phase difference in the light signal that combine either positively or negatively. MZFs are tuned by changing the

physical length of one of the two paths. MZFs are able to realize a narrow passband of less than 0.1 nm, so they are applicable to optical frequency multiplexing (OFDM)[2].

FPFs have a narrow passband of less than 1 nm. Solid type, fiber type, and liquid crystal types of FPFs have been proposed [3][4]. A FPF consists of two highly reflective mirrors separated by a distance. By adjusting the distance between the mirrors, a single wavelength can be chosen to propagate through the cavity, while the remaining wavelengths destructively interfere. The distance between the mirrors can be adjusted mechanically by physically moving the mirrors. The optical crosstalk limits the number of multiplexed channels of FPFs. Also, FPFs are sensitive to temperature changes so that they have to be placed under the temperature control within  $\pm 0.1$  C[5].

AOTFs utilize polarization conversion in wavelength. They are tuned by surface-acoustic waves or interdigital electrodes. This kind of filters appears to be a suitable basis for multi-wavelength optical cross-connects. They offer a broad tuning range, a fast tuning speed, and a simultaneous filtering capability. These filters have polarization dependency and sidelobes with periodic deviation. Researches have been carried out to improve their characteristics [6].

Diffraction grating filters (DGF) are made up of a large number of regularly spaced grooves on a substrate that uses the diffraction property of light and reflects the incident light in a direction that depends on the angle of the incident light, the wavelength and the grating constant. Tuning of DGFs is accomplished by changing the angle of the incident light on the grating. DGFs are widely used on ECL to tune wavelength.

The tunable spectral slicing filter, TSSF, is fabricated on a birefringent electrooptic substrate material. It makes use of phase-matched co-directional polarization conversion in a single mode waveguide for channel selection [8]. This polarization coupling can be achieved via the static strain-optic effect through the use of a dielectric grating overlay film integrated with the waveguide. The spectral slicing feature results from the use of a sparse grating for polarization conversion. The device can be tuned electrooptically or thermally, and is inherently polarization-independent.



Microelectromechanical system (MEMS) based tunable filters are attracting much interest currently because of wide tuning range, polarization insensitive operation and two-dimensional (2-D) array integration [9][10]. One of their drawbacks is the need for a large tuning voltage of several hundreds volts or even larger [11]. In addition, the temperature dependence of resonant wavelength is a remaining problem.

A fiber Bragg grating (FBG) is a piece of fiber with the index of refraction varying periodically along its length. FBG can be made tunable mechanically and thermally. Mechanically, the fiber can be stretched or compressed; hence the Bragg wavelength is tuned. In the thermal tuning, application of heat or cool can change the FBG's length and the index of refraction; thus the Bragg wavelength is tuned. In this thesis work, the mechanical tuning FBG was used to build the optic tunable filter.

## 1.2 Review of FBG-based Filters

The periodic perturbation of the refractive index along the fiber length is formed by the exposure of a bare fiber to an intense interference light pattern.

The formation of permanent gratings in an optical fiber was first demonstrated by Kenneth O. Hill et al. in 1978 [12]. Due to the fiber photosensitivity, the fiber's refractive index changes after UV irradiation. Figure 1.1 shows one FBG writing setup used in Optic Sensing and Communication Laboratory at Ryerson University.

Before radiation, optic fibers need to be loaded in hydrogen to enhance their photosensitivity. The index perturbation in the FBG core (shown in Figure 1.2) is similar to a volume hologram or a crystal lattice, which acts as a stop-band filter. A narrow band of incident optical field within the fiber is reflected by successive, coherent reflection from the index variations. The strongest interaction or mode coupling occurs at the Bragg wavelength  $\lambda_B$  ( $\lambda_{reflect}$  in Figure 1.2) that is given by [18]:

$$\lambda_B = 2n_{eff}\Lambda \quad (1.1)$$

where  $n_{eff}$  is the effective modal index and  $\Lambda$  is the grating period.

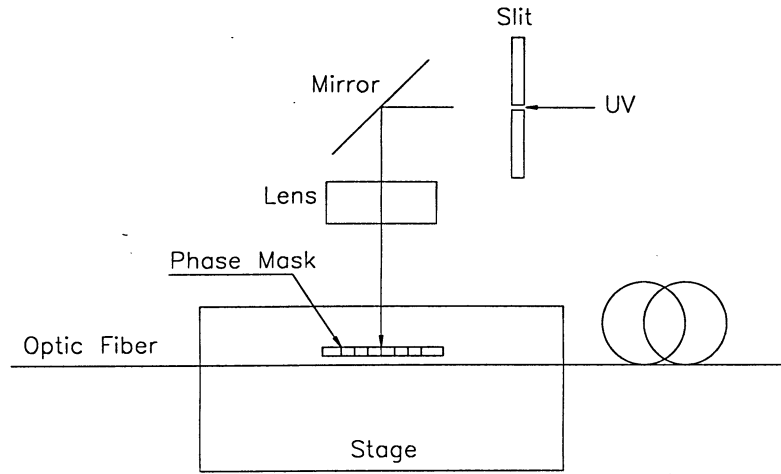


**Figure 1.1:** Scheme of writing a FBG

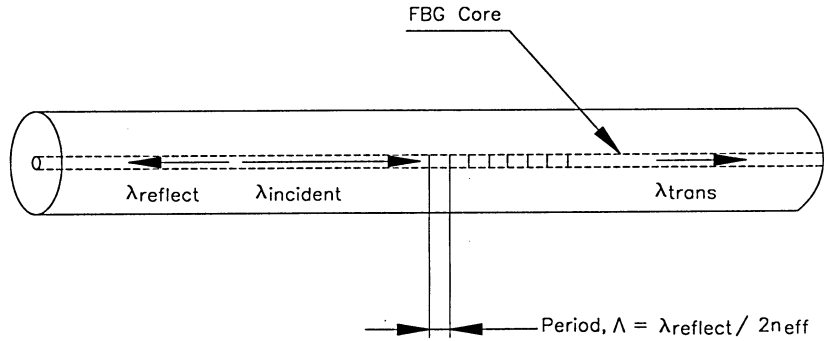


**Figure 1.2:** FBG Core

Currently, there are two main methods to shift the Bragg grating central wavelength : by modifying the fiber refractive index thermally [13][14] or by changing the grating period mechanically [15][16].

Due to the excellent behavior of silica under stress, mechanical stress has been preferentially applied to obtain a wide tuning range. In particular, G.A. Ball et al.

[14] realized a compression based tunable fiber laser over a 32 nm tuning range.

Mechanical stress is applied to the optical fiber along its axial direction by an actuator. The relationship between the stress and the strain in the elastic domain and in the axial direction  $x$  is given by:

$$\sigma_{ax} = E \cdot \varepsilon_{ax} \quad (1.2)$$

where  $E$  is the Modulus of Elasticity of the optic fiber/Silica glass, and  $\varepsilon_{ax}$  is the axial strain which is defined by:

$$\varepsilon_{ax} = \frac{\Delta l_{ax}}{l_{ax}} \quad (1.3)$$

where  $\Delta l_{ax}$  is the change of the guided fiber length,  $l_{ax}$ , under compression. The shift of the Bragg central wavelength,  $\Delta\lambda$ , is related to axial strain by the following relationship [17]:

$$\frac{\Delta\lambda}{\lambda_B} = (1 - \rho_e)\varepsilon_{ax} \quad (1.4)$$

where the photoelastic constant  $\rho_e$  is 0.22 [18].

### 1.3 Motivations

To apply the FBG based optic tunable filters in telecommunication, a significant amount of effort has been put into the filter's design and fabrication in the past years. The majority of these work focused on the filter's tuning resolution, tuning range, and tuning repeatability as shown in Table 1.1. Only few considered the filter's tuning speed, tuning stability, and the thermal effect. However, as shown in [23], these are important issues in practice. Without high tuning speed, the filter can't support the fast switching required in optic communication; without the solution to the thermal drift, the filter can't be deployed in fields.

The goal of this design is to develop a practical tunable optic filter that not only meets the requirement of the tuning resolution, range, and repeatability, but also the requirement of the tuning speed, stability, and thermal stability.

In this thesis, an FBG based tunable filter driven by piezo stacks and stroke expander with a low Coefficient of Thermal Expansion (CTE) was designed. To

References	1 [19]	2 [20]	3 [23]
Structure	PZT+translation stage	Not disclosed	Not disclosed
Closed Loop Switch time	$n/a$	$n/a$	50 ms @Tuning range of 8 nm wavelength error of 50 pm
Tuning Resolution	0.1 nm	$n/a$	$n/a$
Tuning Range	46 nm	45 nm	8 nm
Tuning Repeatability	0.12 nm	$n/a$	$n/a$
Thermal Compensation	$n/a$	$n/a$	70 pm/70 C

**Table 1.1:** A Comparison of FBG-based optic tunable filters from three references

achieve high wavelength stability, a feedback control was employed. To cancel the thermal drift of wavelength, a lower CTE steel, Invar 36, was used to fabricate the actuator. In addition, a thermal compensation mechanism, using two kinds of spacers of different CTEs, was specially designed to compensate for the thermal-induced wavelength drift of the filter. The proposed filter was tested for all the designed features.

Table 1.2 shows the expected characteristics of the filter.

Closed Loop Switch time	<20 ms
Resolution	<10 pm
Maximum Tuning range	20 nm
Repeatability	<50 pm
Thermal Compensation	$\leq 1.5$ pm/C

**Table 1.2:** Characteristics of the tunable filter

## 1.4 Outline of Thesis

The remainder of this thesis consists of three chapters, which are organized as follows:

**Chapter 2:** *Filter Design and Fabrication*, describes the tunable filter's design and fabrication. The calculations, simulations, analysis, drawings, and the assembly are detailed in this chapter. Mechanical design, electronic design, thermal compensation design, Labview programming and filter fabrication are presented in different sections.

**Chapter 3:** *Filter Tests and Measurements*, describes the tests of the filter, including filter calibration, closed loop tuning speed, short and long term drift, wavelength tuning repeatability, tuning resolution, thermal compensation test, and filter applications test. Tests results are discussed in this chapter.

**Chapter 4:** *Conclusions*, discusses the results and summarizes the contributions of this work. Future work on how to improve this filter is proposed.

## Chapter 2

# Filter Design and Fabrication

### 2.1 Introduction

**P**IEZO drive tunable optic filter described in this thesis used two piezo stacks (APC International, Ltd, PZT150 x 10 x 10/20) to generate a stroke of  $0 \sim 40 \mu m$  ( $0 \sim +150$  V DC power supply) or  $0 \sim 60 \mu m$  ( $-30 \sim +150$  V DC power supply). This stroke was magnified by a metal structure, an actuator, which compressed a guided FBG; hence the FBG's Bragg wavelength was shifted. Changing the applied voltage on piezo stacks tuned the FBG's Bragg wavelength. A linear variable displacement transducer (LVDT) (Solartron Metrology, SM1) was used to measure the displacement of the actuator and to provide the feedback control for the filter. This feedback control provided the linear relation between the filter's input and output, and minimized external disturbances [21]. The filter design included mechanical and electronic designs. The mechanical design consisted of the following parts: the actuator, the FBG guiding, the upper and lower holder to fix the guided FBG on the actuator, and the spacers to compensate for the thermal drift of the filter. The electronic design consisted of the following parts: the LVDT driver circuit, the subtractor amplifier (used to build the feedback control with the LVDT), the DC power supply circuit, and PCB Design. A data acquisition (DAQ) card (National Instruments Inc., 6035E) was used to send the control signal from a computer to the subtractor amplifier. Therefore, several Labview programs were also needed to drive the DAQ card, and to perform all the features of the actuator in the application.

## 2.2 Piezo Element

A monolayer structure piezo ceramic, or PZT ceramic (PZT: lead (Pb) zirconia (Zr) Titanate (Ti)), acts as a capacitive element, which is consisted of two thin conductive electrode coatings enclosing the PZT-ceramic as dielectric. When this "piezo-capacitor" (showed in Figure 2.1) is charged by applying a voltage, deformation is created. This deformation is used to produce motions and/or forces. The above effect is the complementary effect to piezoelectricity, where electrical charges are produced upon application of mechanical stress to the ceramics [22].

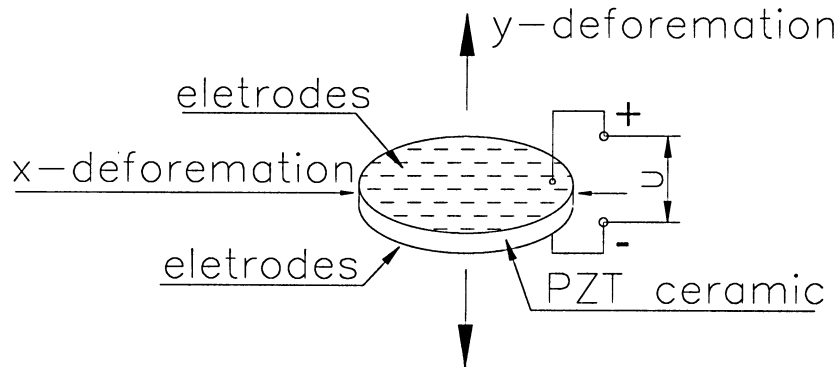


**Figure 2.1:** Schematic of a PZT Single Layer Structure

Piezo stacks make use of the increase of the ceramic thickness in direction of the applied electrical field. Stacking of several layers towards a multilayer structure increases equivalently the total stroke. Stack motion on the order of microns to tens of microns, and force from hundreds to thousands of Newtons are typical [21]. The principal characteristics of the piezo stack are listed as follows: a high energy conversion efficiency, low voltage operation, large force, low motion, a fast response, and no electro magnetic interference (EMI).

Many piezo products based on the multilayer structure have been developed over these years, e.g. piezoelectric motors, sound or ultrasound generating devices [21].

Figure 2.2 shows the diagram of piezo stack's stroke vs. applied voltage used in this thesis. Its open loop sensitivity is approx.  $0.1 \mu\text{m}/1 \text{ V}$  [22].

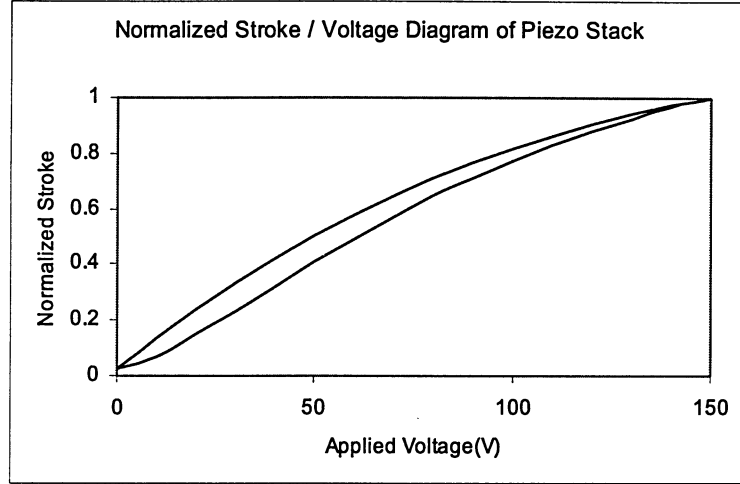


**Figure 2.2:** Stroke/Voltage Diagram of Piezo Stack

From Figure 2.2, the piezo stack's nonlinear error and hysteresis are obvious. Therefore, some methods must be considered to reduce those errors in practice.

## 2.3 Mechanical designs

### 2.3.1 Design Requirement

In this design, a tuning range of 20 nm were expected for a FBG written at 1550 nm. The needed compressed length of fiber for the above target was calculated from Equation 1.4 [17]. Figure 2.3 shows a guided FBG under compression.

Substituting the Bragg wavelength ( $\lambda_B=1550 \text{ nm}$ ), the tuning range ( $\Delta\lambda=20 \text{ nm}$ ), and the guided fiber length ( $l_0=24 \text{ mm}$ ) into Equation 1.4, the required compressed length of fiber,  $\Delta l_{ax}$ , is 0.4 mm.



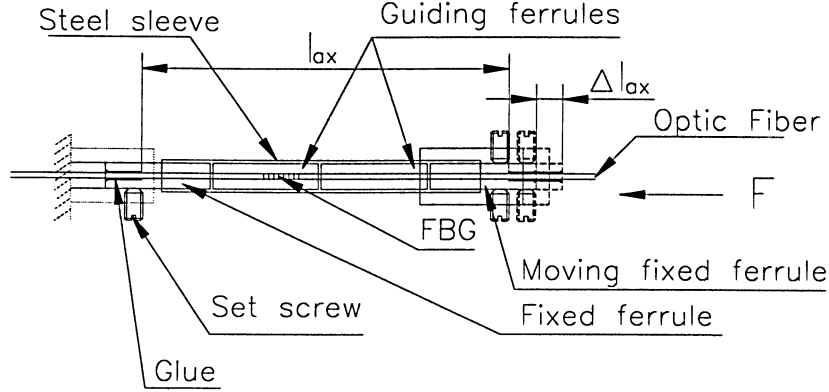


**Figure 2.3: Guided FBG**

From the Equation 2.1, the required force for 0.4 mm fiber compression can be calculated.

$$F = \varepsilon_{ax}EA \quad (2.1)$$

where  $E = 72.5 \text{ GPa}$  is the Modulus of Elasticity of the optic fiber/Silica glass,  $A$  is the section area of fibers. For SMF28 optic fiber with a diameter  $d = 0.125 \text{ mm}$ , its section area,  $A = \frac{\pi d^2}{4}$ , is  $0.0123 \text{ mm}^2$ . Substituting  $A = 0.0123 \text{ mm}^2$  and  $\varepsilon_{ax} = \frac{\Delta l_{ax}}{l_0} = \frac{0.4 \text{ mm}}{24 \text{ mm}} = 1.1\%$  into Equation 2.1, the required force is  $F = 14.5 \text{ N}$ .

To minimize the thermal effect on the structure, Invar 36 was selected to build the actuator. Invar 36 is a 36 % nickel-iron alloy which has a low thermal expansion from room temperature to approximately 230 C.

High durability is an additional requirement in this design, because this optic filter is expected to operate more than one million times. Studies carried out by Boeing Inc. show that Invar 36 is the material which provides the best compromise between the CTE, durability and overall fabrication costs [24][25].

To ensure the durability of the actuator, the maximum strain on the actuator,  $S_f$ , should not exceed the fatigue strength. It can be calculated from:  $S_f = \frac{T_Y \times 0.6}{E}$ , where  $T_Y = 679 \text{ MPa}$  is the yield tensile strength of Invar 36, and  $E = 148 \text{ GPa}$  is

the modulus of elasticity of Invar 36. Therefore, the maximum strain is  $S_f = 2752 \mu\epsilon$ .

Table 2.1 shows the properties of materials and piezo stacks used in this design.

Material	M. of Elasticity (GPa)	$\alpha$ ,CTE (ppm/C)	Poisson's Ratio	Shear M.(GPa)	Tensile S. Yield(MPa)
Type 430 Stainless Steel	200	10.4, 0-100C	0.29	86	441
Type 304 Stainless Steel	200	17.3, 0-100C	0.29	86	205
Invar 36 (cold drawn)	148	1.3, 20-100C	0.3	60	679
Invar 36 (annealed)	141	0.96, 20-100C	0.3	60	274
Zn	96.5	31, 0-100C	0.249	38.6	35
Piezo stack	90	-4.5, 0-100C	0.31	58	
Optic Fiber (Silica glass)	72.5	0.55,0-250C	0.19	30	3310

**Table 2.1:** Material properties

### 2.3.2 Finite Element Analysis of Actuator

Since the maximum stroke generated by two piezo stacks was only  $40\mu m$  ( $0 \sim 150$  V power supply), the stroke gain of 10 was needed to magnify the piezo stroke to the required compressed length of the fiber, 0.4 mm, under a load of 14.5 N. An elastic elliptical shell actuator truncated in the long axis, with piezo-actuation in its long axis and an amplified stroke in its short axis, was designed to achieve a stroke gain as described in [26]. This kind of structure provided negligible backlash, noise-free, no need of lubricants and no wear motion [28]. The stroke gain of that actuator on a zero force load is the ratio of length of its long axis to its short axis. However, it was not practical to design and fabricate an elliptical shell actuator with a gain of 10 on 14.5 N load, due to its very large size. In this thesis design, flexural-hinges on the elliptical shell actuator were used to achieve a sufficient stroke gain [27]. Figure 2.4 shows the structure of the half actuator with 8 flexural-hinges.

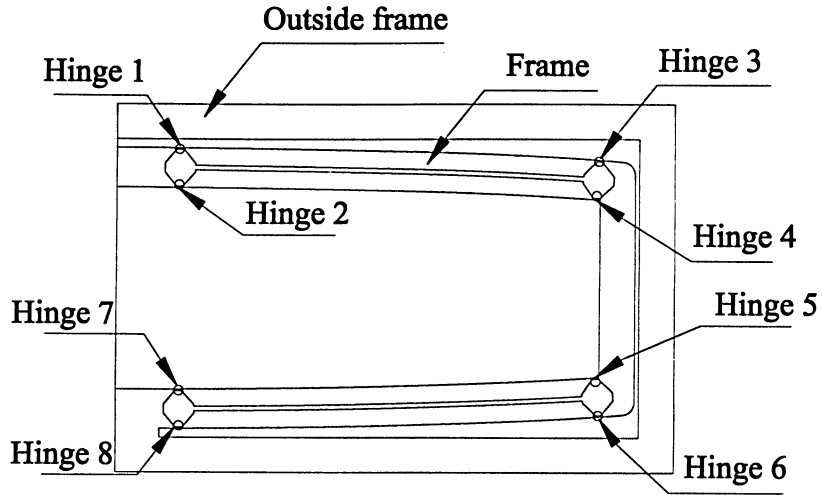


**Figure 2.4:** Half actuator with 8 flexural-hinges

In the actuator design, the Finite Element Analysis (FEA) software, ANSYS , was used to analyze the actuator's mechanics model, and to optimize the actuator's structure in order to achieve the required stroke gain and force. Figure 2.5 shows the ANSYS 3D-model of the actuator. Due to the symmetry of the structure, only a half of the actuator model was built and analyzed in ANSYS to reduce the amount of calculation data; hence, the piezo stroke applied on the actuator in the x-direction was half of the two piezo strokes. The outside frame shown in Figure 2.4 was not included in ANSYS models, since it was stationary, and had no effect on the actuator's mechanical structure.

Figure 2.6 shows the model after meshing. The ANSYS element type, SOLID 95, was selected to build the model. It is a higher order version of the 3-D 8-node solid element, SOLID45. The hinges have curved surfaces. Compared to SOLID 45, SOLID 95 is well suited to models with curved boundaries [37]. It can tolerate irregular shapes without losing accuracy.

The boundary condition was defined as follows (shown in Figure 2.7):

- Area 1 and 2 on the model can't move in the x-direction due to the symmetry of the actuator. They connect the other half model. Therefore, their displacement

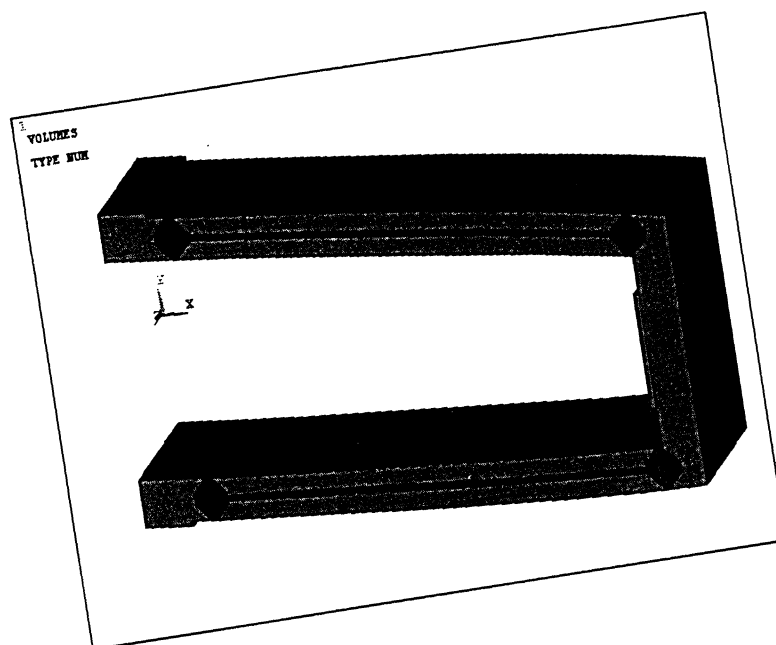


Figure 2.5: 3-D actuator

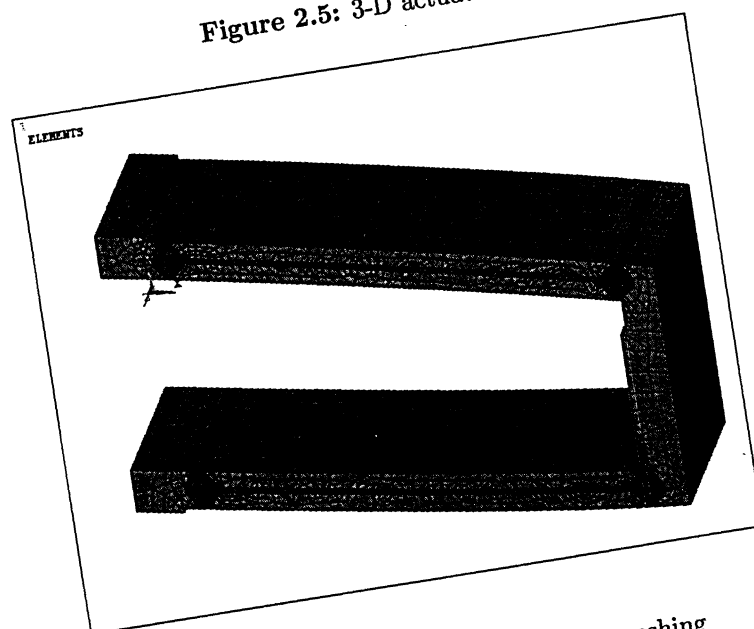
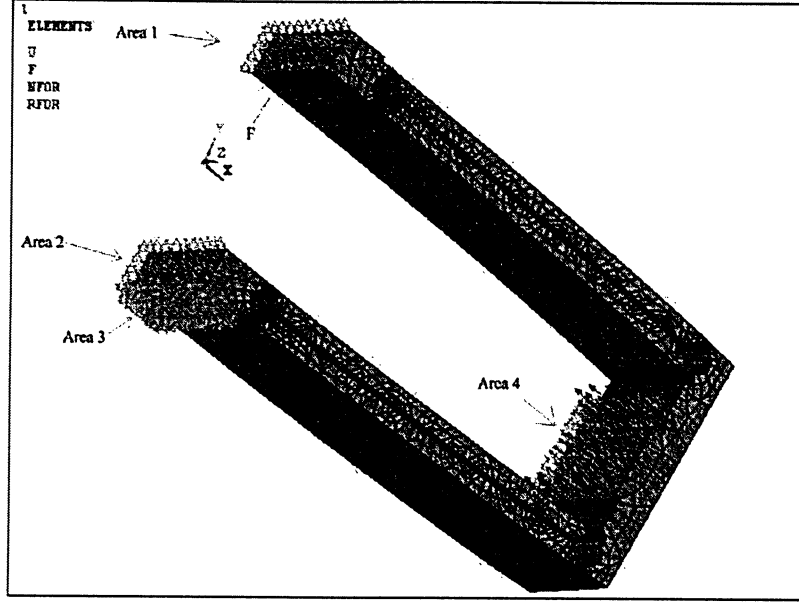


Figure 2.6: Model of actuator after meshing

in the x-direction is 0.

- Area 3 on the model connects to the outside frame of the actuator. It is the reference area of the model in the y-direction in ANSYS. The displacement of this area in the y-direction is 0.



**Figure 2.7:** Boundary Condition

- Piezo stacks generates  $20 \mu m$  displacement and it is the load applied on the area 4.
- Force "F" is applied in the frame's y-axis on the model. It is the reaction force of the compressed FBG, which is equal, but in opposite direction, to the force that is generated by the frame when the frame is deformed.

Table 2.2 shows the main results of the ANSYS analysis of the frame with  $F=0$ , where  $\Delta x$  is the applied displacement in the model's x-axis,  $\Delta y$  is the frame displacement in the y-direction,  $(\Delta y/\Delta x)$  is the stroke gain, and  $(S_{max}(x))$  is the maximum tensile strain in the frame's x-direction.

From these results, the actuator's stroke gain is between 30.85 - 30.9, and the difference in gain is less than 0.2%. The negative means  $\Delta y$  decreases along the y-direction when  $\Delta x$  increases in the x-direction. The maximum strain is perfectly a linear function of  $\Delta x$ , i.e. the whole structure works in the linear region. The maximum strain under  $\Delta x = 25 \mu m$  (-15 ~ +150 V applied voltage on the piezo stack) is - 1814  $\mu\epsilon$ , and negative means tensile strain. It is less than the fatigue

strength of the actuator,  $S_f=2752 \mu\epsilon$ . Figure 2.8 shows the structure deformation.

$\Delta x(\mu m)$	5	10	15	20	25
$\Delta y(\mu m)$	-309	-617	-926	-1234	-1543
$\Delta y/\Delta x$	-30.9	-30.85	-30.87	-30.85	-30.86
$S_{max}(x)(\mu\epsilon)$	-343	-686	-1028	-1371	-1814

**Table 2.2:** Structure deformation

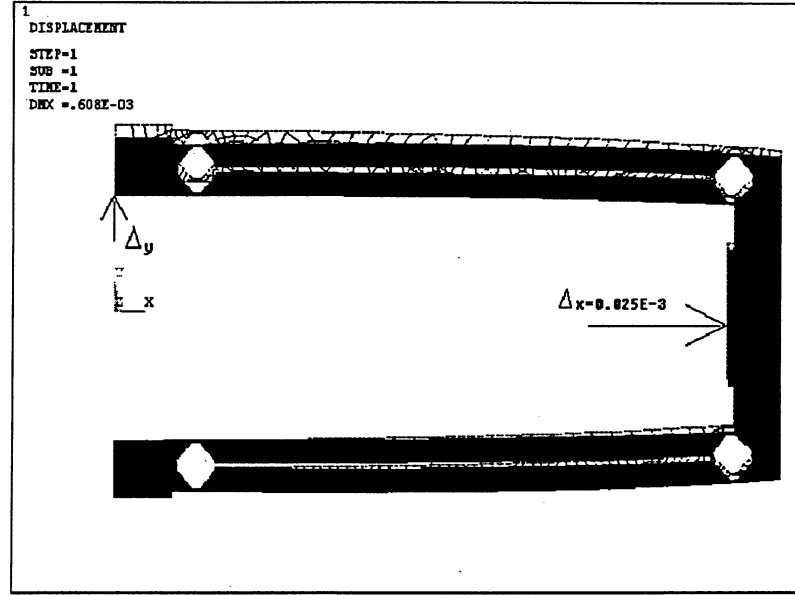


**Figure 2.8:** Structure deformation under  $U_x = 25 \mu m$

ANSYS was also used to optimize the model in this section. Before optimization, those hinges on the actuator had the same length and thickness. From the second column of Table 2.3, it can be seen that the difference of the maximum strain among the hinges is  $804 \mu\epsilon$ . The goal of the optimization was to balance this maximum difference of strains.

Depend on the ANSYS analysis results, the length and thickness of hinges were changed to balance the strains on those hinges. In the optimization, the piezo stack's stroke,  $\Delta x = 25 \mu m$ , was used on all models, and the thickness of the actuator was

15.8 mm. Table 2.3 shows the dimension of the hinges and the maximum strains on hinges before and after optimization.

Hinge	$S_{max(x)}(\mu\epsilon)$ , before Op.	$S_{max(x)}(\mu\epsilon)$ , after Op.	Thickness( $\mu m$ )	Length(mm)
1	-1051	-1590	180	0.88
2	-1394	-1620	170	0.79
3	-1814	-1707	180	0.59
4	-1576	-1690	170	0.74
5	-1584	-1650	170	0.74
6	-1855	-1714	180	0.59
7	-1388	-1610	170	0.79
8	-1010	-1580	180	0.88

**Table 2.3:** Hinge optimization

After optimization, the difference of  $S_{max(x)}$  on hinges was reduced from 804  $\mu\epsilon$  to 134  $\mu\epsilon$ . The maximum strain on the actuator is -1714  $\mu\epsilon$ , which is less than the fatigue strength of the actuator,  $S_f=2752 \mu\epsilon$ .

Table 2.4 shows the deformation of the actuator for the different forces and a fix displacement in the x-axis,  $\Delta x = 25 \mu m$ . From the table, it can be seen that  $\Delta y$  decreases as the force increases.

Force (N)	10	12	20	28	28*
$\Delta y(\mu m)$	-1071	-982	-609	-250	-586
Gain	21.4	19.6	12.18	5	11.72
$S_{max(x)}(\mu\epsilon)$	-718	-880	-1243	-1630	-1723

**Table 2.4:** Force vs. Deformation

The last column in Table 2.4 shows the displacement  $\Delta y$  if the actuator material was changed from Invar 36 to Type 304 stainless steel on the same model. The stroke gain is significantly large at the same load and boundary condition if Type 304 stainless steel was used, due to the higher modulus of elasticity of Type 304 than that of Invar 36.

From the ANSYS results, the displacement in y-direction,  $\Delta y$ , was 825  $\mu m$  under force=14.5 N, and the maximum strain on the hinge ,  $S_{max(x)}$ , was -1714  $\mu\epsilon$ . This result meets the requirements described in Section 2.3.1.

### 2.3.3 Mechanical Design of Actuator

The engineering drawing of the actuator is made using Autocad as shown in Figure 2.9. The structure of the actuator frame and flexible hinges were calculated based on the ANSYS results. An outside frame was design to provide a base for the actuator. The holes 1-8 on the outside frame were designed to install the actuator's top and bottom covers. Because of machining tolerance, the tight contacts between spacers, piezo stacks and the actuator requires a pre-load. The tapped holes of 9-16 were designed to hold four springs to provide the pre-load. The guided FBG was fixed on the actuator by the upper holder and the lower holder through the center holes of 23 and 24. The tapped holes of 17, 18, 19, and 20 were used to connect the upper and lower holders to the actuator by screws. The holes of 21 and 22 are two spare holes for providing an extra pre-load if needed. Two slots (Slot 1 and 2) with one end open and the other one end closed were designed to retain spacers for applying load and thermal compensation.

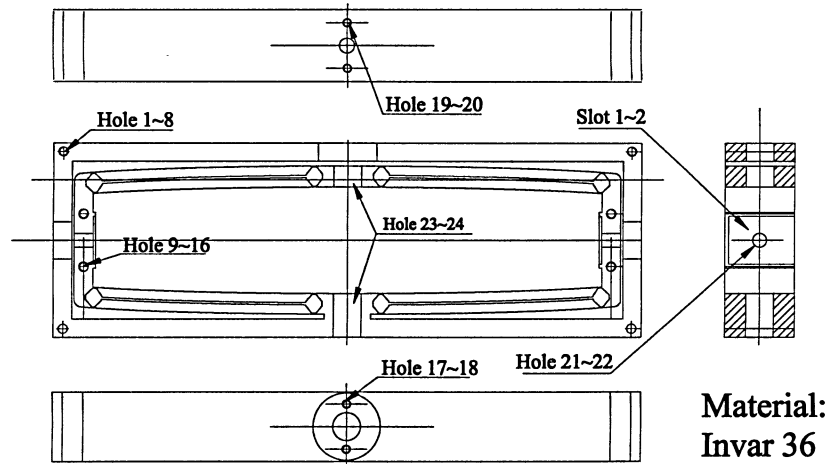
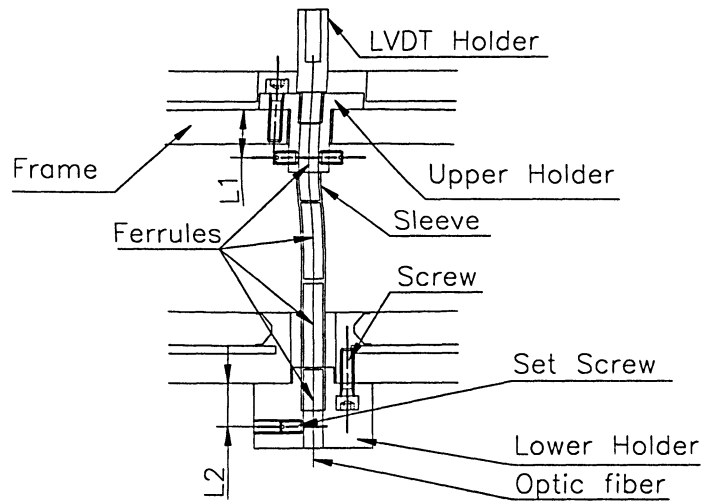


Figure 2.9: Actuator

### 2.3.4 Mechanical Design of FBG guiding

FBG guiding assembly and a part of the actuator are showed in Figure 2.10. An





**Figure 2.10:** Accessorial parts of the actuator

LVDT holder was designed to install the LVDT rod on the same line of the y-axis of actuator. The high concentricity of the LVDT rod fitting with the upper holder is required to reduce the error of the LVDT measurement.

The optic fiber was guided in four ferrules, each with a length of 10.5mm, and was glued inside the two end ferrules. A precisely machined sleeve was designed to hold these four ferrules. Lower holder and Upper holder were designed to fix the two end-glued ferrules in the assembly by four set screws. The requirement of the holders was to keep  $L1=L2$  (shown in Figure 2.10 ). In this case, those two holders had the same thermal expansion in same direction. These two thermal expansions counteracted each other in the following thermal compensation design. In addition, the high concentricity of the upper and lower holders fit with the hole of 23 and 24 (shown in Figure 2.9) was required. The fit of G7/h6 based on the shaft basis system was required for the sleeve and holders.

## 2.4 Thermal Compensation Design

### 2.4.1 Introduction

When an FBG-based tunable optic filter operates in an environment with a variable temperature, its center wavelength will shift with temperature [29]. For example, an FBG made of SMF 28 fiber and written at 1550 nm will shift at a rate of 10 pm/C. The thermal expansion of the actuator frame will change the distance between the upper and lower holders. This will further shift the FBG wavelength. It is a challenge to analyze the whole thermal effect of the filter because it combines the thermal expansion of the actuator and the thermal shift of the FBG's refractive index. In this thesis, two kind of spacers with different CTEs, Spacer A and Spacer B, were designed to compensate for this thermal effect of the filter.

Figure 2.11 shows the actuator thermal compensation design. Spacers generated

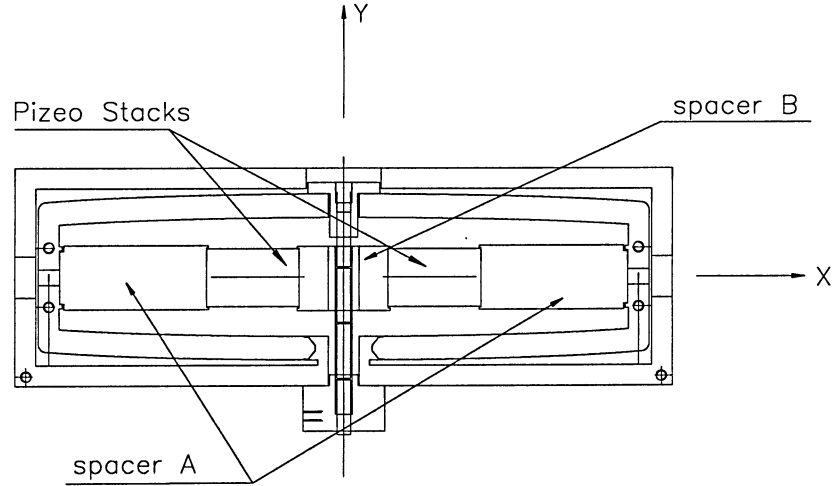


**Figure 2.11:** Thermal compensation structure

an additional thermal expansion or contraction in the actuator's x-direction when the temperature changed. This x-axis length change of the actuator changed the length of the actuator in the y-direction; hence the FBG was compressed or elongated, and the Bragg wavelength shift due to the thermal effect was compensated.

ANSYS was used in the thermal compensation design to calculate the thermal deformation of the actuator, spacers and piezo stacks.

### 2.4.2 Actuator Thermal Effect Analysis

Figure 2.12 shows the thermal effect of the actuator with a +10 C temperature change applied on the model. Other boundary conditions were defined the same as in Section 2.3.2. In Figure 2.12, the scale of deformation is enlarged to 1000:1. From the ANSYS

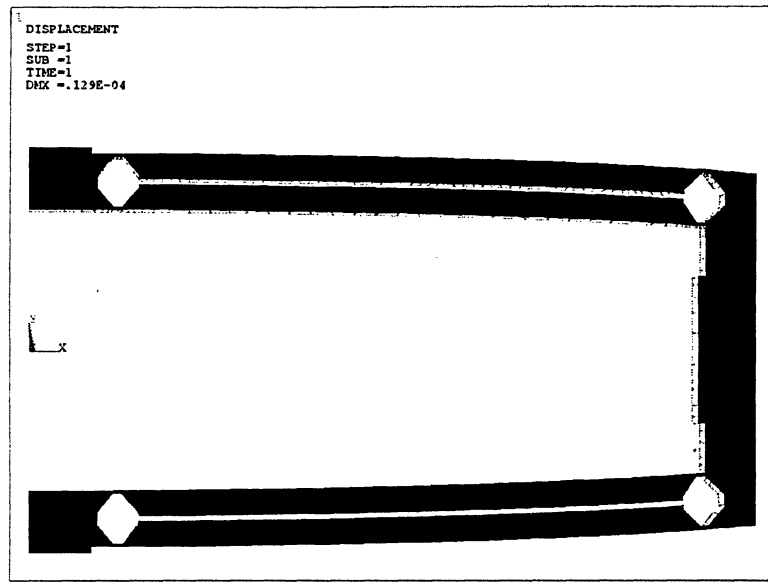


**Figure 2.12:** ANSYS result of the thermal effect on the actuator

result, the x-axis and y-axis thermal expansions of the frame were:

$$\Delta l_{x(F|T)} = 1.05 \mu m / 10 C \quad (2.2)$$

$$\Delta l_{y(F|T)} = 0.297 \mu m / 10 C \quad (2.3)$$

The model of the actuator frame without hinges was also built to make a comparison. Figure 2.13 shows the the model of this frame, in which hinges were replaced by solid bars. ANSYS gave the thermal expansions of the frame without hinges:

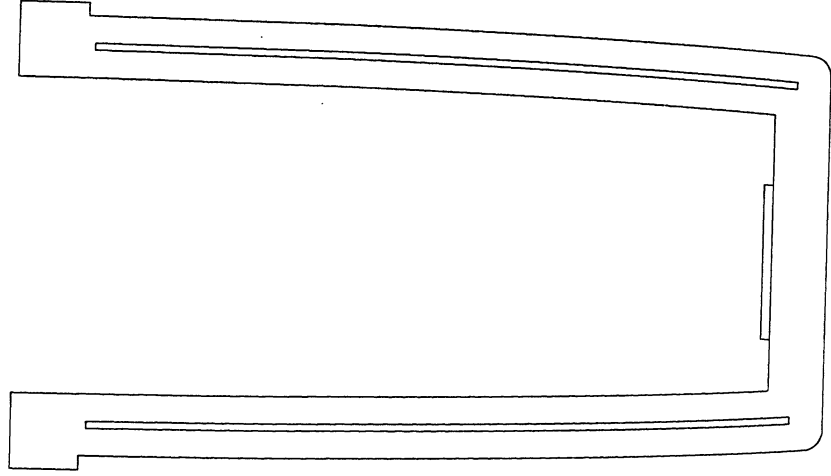


**Figure 2.13:** Frame without flexible hinges

$$\Delta l_{x(F|T)} = 1.045 \mu m / 10C \quad (2.4)$$

$$\Delta l_{y(F|T)} = 0.383 \mu m / 10C \quad (2.5)$$

If simply using the following thermal expansion equation:

$$\Delta l = L \cdot \alpha \cdot \Delta T \quad (2.6)$$

to calculate the frame's thermal expansions, the x-axis and y-axis thermal expansions of the frame are:

$$\Delta l_{x(F|T)} = 1.054 \mu m / 10C \quad (2.7)$$

$$\Delta l_{y(F|T)} = 0.378 \mu m / 10C \quad (2.8)$$

The result from Equation 2.6 is close to the ANSYS result of the frame without hinges. Comparing ANSYS results of these two frames, it is seen that the flexural-hinges reduces the thermal expansion in the actuator's y-direction by 21.4%, and gives no change in the x-direction. It is obvious that the flexible hinges increases the complexity of the thermal effect calculation of the actuator.

### 2.4.3 Spacers Calculation and Design

The temperature characteristic of FBG is given by [18]:

$$\frac{\Delta\lambda_T}{\lambda_B} = (\alpha + \zeta)\Delta T \quad (2.9)$$

where  $\alpha = (1/\lambda)(\partial\lambda/\partial T)$  is the CTE of optic fiber;  $\zeta = (1/n_{eff})(\partial n_{eff}/\partial T)$  is thermo-optic coefficient. For Silica glass,  $\alpha$  is 0.55 ppm/C, and  $\zeta$  is 6.6 ppm/C. For the FBG made of SMF 28 optic fiber,  $\Delta\lambda_T$  is 0.1 nm/10 C at 1550 nm. Therefore, in this design, the FBG needs to be compressed to achieve a -0.1 nm/10 C Bragg wavelength shift,  $\Delta\lambda_s$ , to realize the thermal compensation. Figure 2.14 defines the symbols used in the thermal compensation calculation.

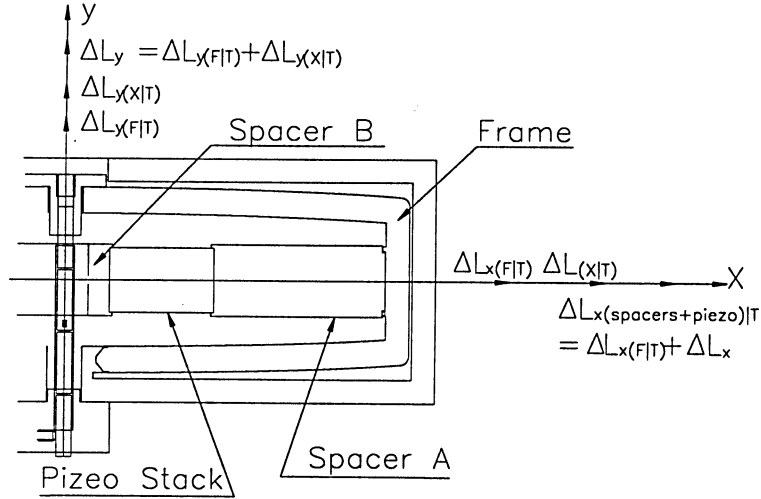


**Figure 2.14:** Actuator thermal effect calculation

First,  $\Delta l_y$ , the compressed fiber length to compensate for the thermal drift of an FBG, is to be calculated from the following equation:

$$\Delta l_y = \frac{\Delta\lambda_s}{\lambda_B(1 - \rho_e)} l_0 \quad (2.10)$$

where the photoelastic constant  $\rho_e = 0.22$ , Bragg wavelength  $\lambda_B = 1550$  nm, and the guided FBG length  $l_0 = 24$  mm. Substituting  $\Delta\lambda_s = -0.1$  nm/10 C into Equation 2.10,  $\Delta l_y$  is -1.98  $\mu\text{m}/10\text{C}$ .

The total compression in the y-axis,  $\Delta l_y$ , is the sum of the thermal expansion of the actuator frame along the y-axis,  $\Delta l_{y(F|T)} = 0.297 \mu m/10C$  (described in Section: 2.4.2), and the deformation of the actuator frame along the y-axis due to the thermal expansion of the actuator frame along the x-axis,  $\Delta l_{y(X|T)}$ ,

$$\Delta l_y = \Delta l_{y(F|T)} + \Delta l_{y(X|T)} \quad (2.11)$$

Hence,

$$\Delta l_{y(X|T)} = \Delta l_y - \Delta l_{y(F|T)} = -2.28 \mu m/10C \quad (2.12)$$

From the actuator calibration of  $\Delta y/\Delta x$  under the force load (the actuator with the guided FBG), and 60 V piezo driver output, the displacement gain of the half actuator is -4.88. Therefore, the deformation of the actuator's x-axis,  $\Delta l_{X|T}$ , which generates  $\Delta l_{y(X|T)}$ , is

$$\Delta l_{y(X|T)} / -4.88 = 0.467 \mu m/10C \quad (2.13)$$

The expansion of the spacers and piezo stacks,  $\Delta l_{x(s)|T}$  ( $\Delta l_{x(spacers+piezo)|T}$  in Figure 2.14), includes two parts: one is the thermal expansion of the frame in x-axis,  $\Delta l_{x(F|T)}$ ; the other is the required deformation,  $\Delta l_{X|T}$ . Therefore,

$$\Delta l_{x(s)|T} = \Delta l_{x(F|T)} + \Delta l_{X|T} \quad (2.14)$$

Substituting  $\Delta l_{X|T} = 0.467 \mu m/10C$ , and  $\Delta l_{x(F|T)} = 1.05 \mu m/10C$  (Section: 2.4.2) into above equation,  $\Delta l_{x(s)|T}$  is  $1.517 \mu m/10C$ .

The spacer A was made of Invar 36, and spacer B was made of Type 304 stainless steel. The length of spacer A and B,  $l_A$  and  $l_B$ , can't be simply calculated from Equation 2.6, because the aperture in the center of the spacer B changes the thermal expansion of the spacer B. Figure 2.15 shows the ANSYS analysis of the thermal expansion of the spacers and piezo stacks. From this figure, the spacer B has the biggest thermal expansion at the spot with the thinnest wall. The expansion difference on the space B decreases if the aperture's diameter is small with respect to the length of spacer B. The thermal deformation of the spacer B was well calculated in ANSYS.

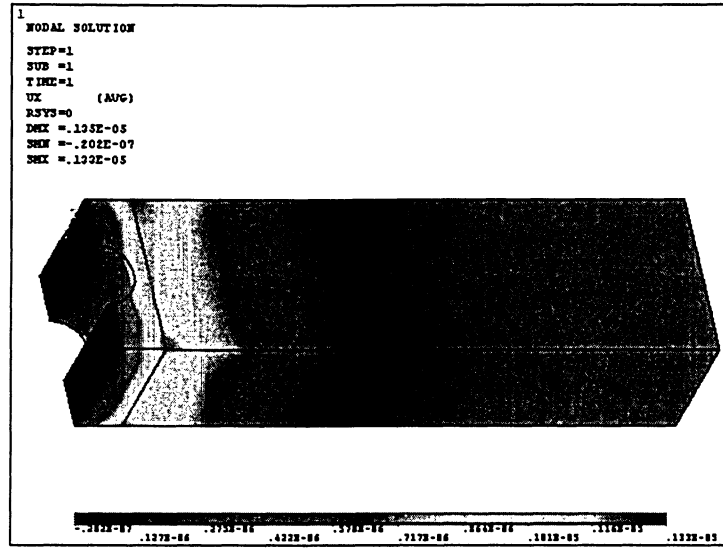


**Figure 2.15:** Thermal expansion of spacers and piezo stacks (x-direction)

From ANSYS results,  $\Delta l_{x(s)}|_T = 1.517 \mu\text{m}/10^\circ\text{C}$  was obtained when the length of spacers,  $l_A$  and  $l_B$ , were 29.17 mm and 15.46 mm, respectively.

Slots and stages on these two spacers were designed to retain the piezo stacks and spacers in the frame.

## 2.5 Electronic Designs

The electronic control system was designed for two purposes: to measure the displacement, and to tune the filter to a required wavelength with a feedback control. Figure 2.16 shows the electronic block diagram of the filter. The electronic design includes four parts: the driver circuit of the LVDT; a subtractor amplifier; a low noise DC power supply circuit; the printed circuit board (PCB). The requirements of the electronic circuit design are high linearity,  $1/25000$ ; low noise,  $<30 \mu\text{V}$ ; low drift,  $<100 \text{ ppm}/^\circ\text{C}$ .

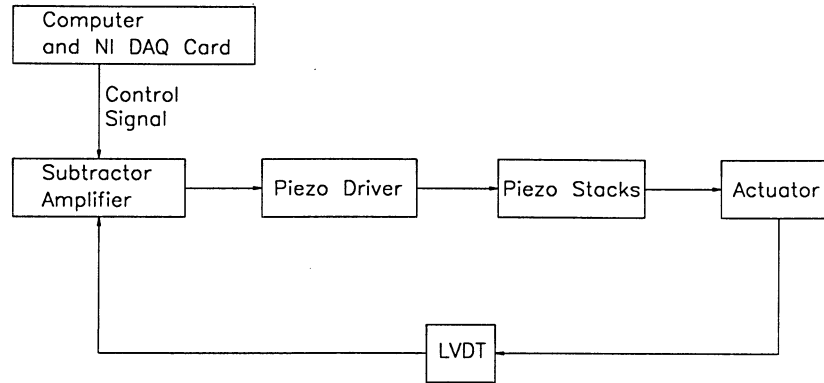


**Figure 2.16:** Electronic block diagram of the tunable filter

### 2.5.1 LVDT Driver Circuit Design

Linear Variable Differential Transformer (LVDT) is an electromechanical transducer that produces an AC voltage output proportional to the relative displacement of the core and the windings.

LVDT's input is the mechanical displacement of a core, and its output is an AC voltage proportional to core position. Figure 2.17 illustrates the function of an LVDT. The moveable core couples flux between the windings. The series-opposed connected

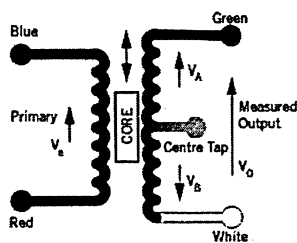


**Figure 2.17:** LVDT

LVDT transducer consists of a primary winding energized by an external sinusoid wave reference source and two secondary windings connected in the series opposed configuration. With the core in a central position, the coupling from the primary



$V_e$  to each secondary is equal, so  $V_A = V_B$  and the output  $V_o = 0$ . As the core is displaced,  $V_A$  differs from  $V_B$  in proportion to the displacement; hence  $V_o$  changes in magnitude and phase in proportion to movement in either direction from null. The direction of movement is detected by measuring the phase of the output.

The main advantage of the LVDT principle over other types of displacement transducer is its high degree of robustness. This is derived from their principle in which there is no physical contact across the sensing element, hence zero wear in the sensing element. The LVDT principle of measurement is based on magnetic transfer which also means that the resolution of LVDT transducers could be infinite. The smallest fraction of movement can be detected by suitable signal conditioning electronics.

Figure 2.18 shows the application of LVDT driven by an AD698 subsystem, a signal conditioner.

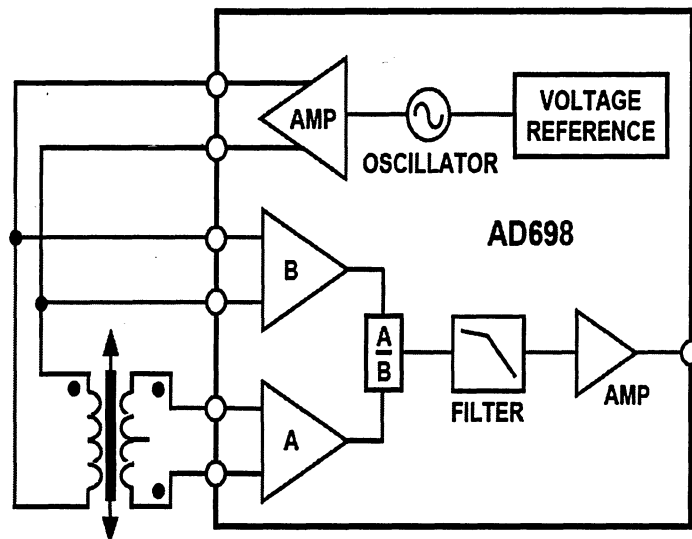


**Figure 2.18:** LVDT driven by a signal conditioner

The AD698 chip is a complete, monolithic LVDT signal conditioning subsystem. It is widely used in conjunction with LVDTs to convert transducer mechanical position to a unipolar or bipolar DC voltage with excellent accuracy and repeatability. With the addition of external passive components to set frequency and gain, the AD698 converts the raw LVDT output to a scaled DC signal. The AD698 contains

a low distortion sine wave oscillator to drive the LVDT primary. Two synchronous demodulation channels of the AD698 are used to detect primary and secondary amplitudes, respectively. The part divides the output of the secondary by the amplitude of the primary and multiplies by a scale factor. This eliminates scale factor errors due to drift in the amplitude of the primary drive, improving temperature performance and stability. The AD698 uses a unique ratio metric architecture such that primary to secondary phase shifts and transducer null voltage have no effect on overall circuit performance. The benefits of this circuit are: no adjustment, higher temperature stability, and higher transducer interchangeability. The AD698 is available in two performance grades: AP, SQ [30]. SQ was selected in this design.

Figure 2.19 shows the connection method of 4-wire LVDT connected in the series opposed configuration with a  $\pm 15$  V power supply. The design of the LVDT

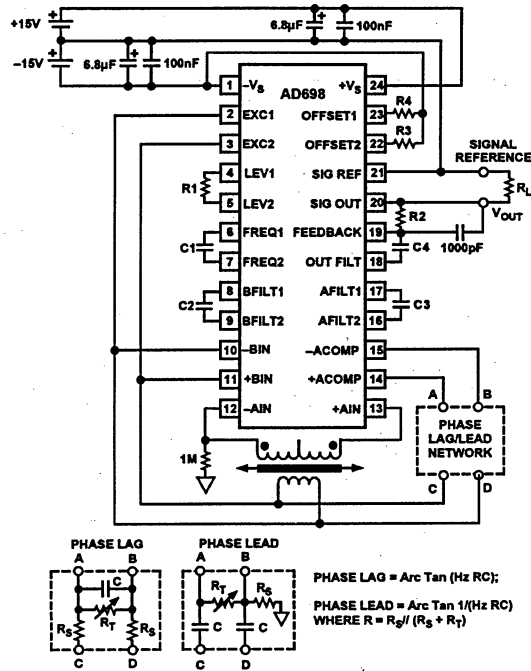


Figure 2.19: LVDT driven by AD698

drive circuit includes the following calculations: the excitation frequency determining capacitor C1; the oscillator amplitude determining resistor R1; the optimum LVDT excitation voltage,  $V_{EXC}$ ; C2, C3 and C4 for the desired bandwidth of the AD698

position measurement subsystem; R2, for the full-scale output voltage. R3 and R4 are set for the offset of output voltage swing. R3, R4 and the phase lag/lead circuit were fixed after the PCB assembly and pre-test.

The energizing frequency of the LVDT,  $f_{EXC}$  was set to match the LVDT zero phase frequency. C1 is given by [30]:

$$C1 = \frac{35\mu F}{f_{EXC}} \quad (2.15)$$

From the LVDT's datasheets, the zero phase frequency of the LVDT was at 14 kHz. Therefore, C1 was 0.0025  $\mu F$ .

The oscillator amplitude is set such that the primary signal is in the range of 1.0 V to 7 V rms and the secondary signal is in the range of 0.25 V to 7 V rms when the LVDT is at its mechanical full-scale position. This optimizes linearity and minimized noise susceptibility.

The voltage transformation ratio of the LVDT at its mechanical full scale, VTR, is determined by  $VTR = \delta \times l$ , where  $\delta$  is the LVDT sensitivity and  $l$  is the maximum stroke length from null of LVDT, for LVDT SM1,  $\delta$  is 0.148 V/V/mm and  $l$  is  $\pm 1.5$  mm, VTR is 0.222. With  $\pm 18$  V power supply, the maximum excitation,  $V_{EXC}$ , is 7 V rms, the maximum secondary voltage will be  $7V \text{ rms} \times 0.222 = 1.55$  V rms, which is in the acceptable range. When  $V_{EXC}$  is 7 V rms, the the value of the amplitude determining component R1 is selected as 4 k $\Omega$  by the curve shown in Figure 2.20 [30].

The system bandwidth,  $S_f$ , was expected to be 250 Hz. C2, C3, and C4 are functions of the system bandwidth. They have nominally equal values, and are determined by the Equation 2.17:

$$C2 = C3 = C4 = 10^{-4}(F)(Hz)/S_f(Hz) \quad (2.16)$$

Substituting  $s_f=250$  Hz into the above equation, C2, C3, and C4 equals 0.4  $\mu F$ . When selecting values of C2, C3 and C4, a trade-off is involved. There is ripple on the "DC" position output voltage, and the magnitude is determined by the filter capacitors. Generally, smaller capacitors would give higher system bandwidth and

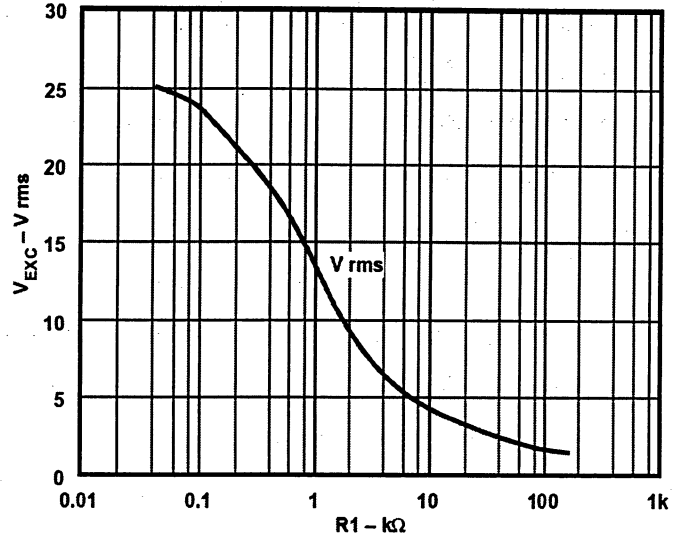


**Figure 2.20:** Excitation voltage  $V_{EXC}$  vs.  $R1$

larger ripple. Figures 2.21 [30] shows the magnitude of ripple as a function of  $C2$ ,  $C3$  and  $C4$ , again all equal in value. A shunt capacitor across  $R2$ ,  $C_{shunt}=10$  nF, was used as an additional filter to reduce the ripple. This would increase phase lag.

$R2$  is given by [30]:

$$R2 = \frac{V_{out}}{\delta \times d \times 500\mu A} \quad (2.17)$$

where  $V_{out} = \pm 7$  V is full-scale range (14 V span), and  $d$  is the full-scale displacement of LVDT, 3 mm. Solving the Equation 2.17,  $R2$  is 63 kΩ.

A 5 V precision voltage reference transducer, REF02(Burr-Brown Co., REF02BP), was used to provide a precision voltage reference for AD698. Figure 2.22 shows this voltage reference circuit. The features of this voltage reference circuit are the following: output voltage noise  $< 2.5 \mu V_{p-p}$ ; temperature stability  $< 10$  ppm/C, 2000hrs term drift  $< 30$  ppm.

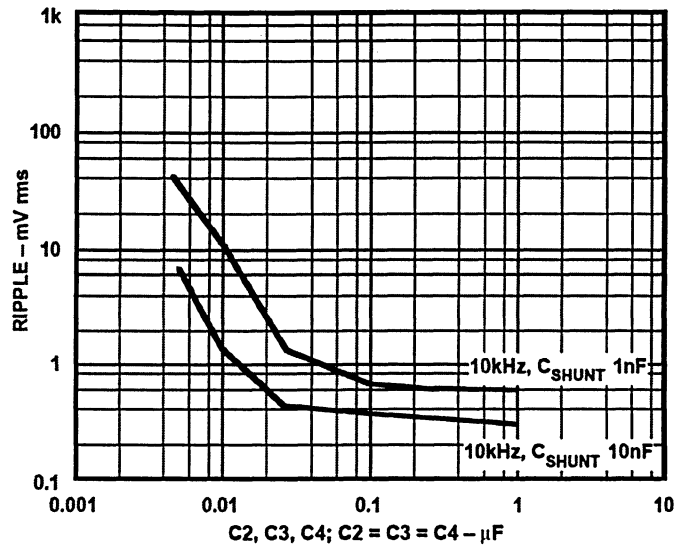


Figure 2.21: Output voltage ripple vs. Filter Capacitance

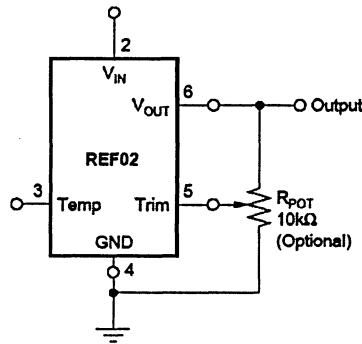
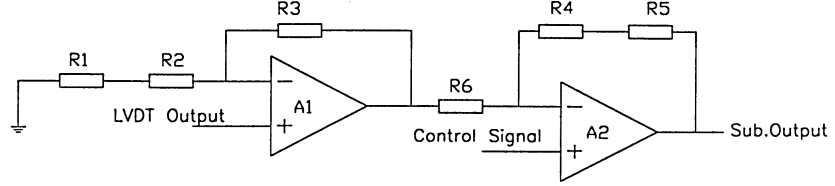


Figure 2.22: +5V Reference

## 2.5.2 Subtractor Amplifier Design

The subtractor amplifier was used in the design to build the feedback in a closed-loop with the LVDT. Figure 2.23 shows the circuit.

This subtractor required that  $R_1 + R_2 = R_4 + R_5$ , and  $R_3 = R_6$ ; thus the subtractor's



**Figure 2.23: Subtractor**

output,  $V_{Sub,O}$ , is given by:

$$V_{Sub,O} = \left(1 + \frac{R4 + R5}{R3}\right)(V_{Contr} - V_{LVDT,O}) \quad (2.18)$$

where,  $V_{Contr}$  is the control signal, and  $V_{LVDT,O}$  is the LVDT output. Six 9.4 k $\Omega$  resistors with 5  $\Omega$  difference were selected for R1, R2, R3, R4, R5, and R6; hence  $V_{Sub,O} = 3 \times (V_{Contr} - V_{LVDT,O})$ . This subtractor also requires that the two operational amplifiers have a higher common mode rejection ratio (CMRR). An operational amplifier, LTC1150 (Linear Technology Corporation, LTC1150CN8), was selected to build the subtractor. LTC1150 is a high-voltage  $\pm 16$  V, low offset 0.5  $\mu V$ , low noise 1.8  $\mu V_{p-p}$ , high-performance (CMRR > 130 dB), and zero-drift < 0.01  $\mu V/C$  operational amplifier [31].

### 2.5.3 Low Noise DC Power Supply Circuit Design

In this filter, the whole circuit system was powered by a  $\pm 18$  V DC power supply. To reduce the noise on the DC circuit, which mainly comes from the AC circuit and the power wires, an additional low noise DC power supply with  $\pm 15$  V output was designed for the DC circuit. Figure 2.24 shows the DC power supply for the subtractor.

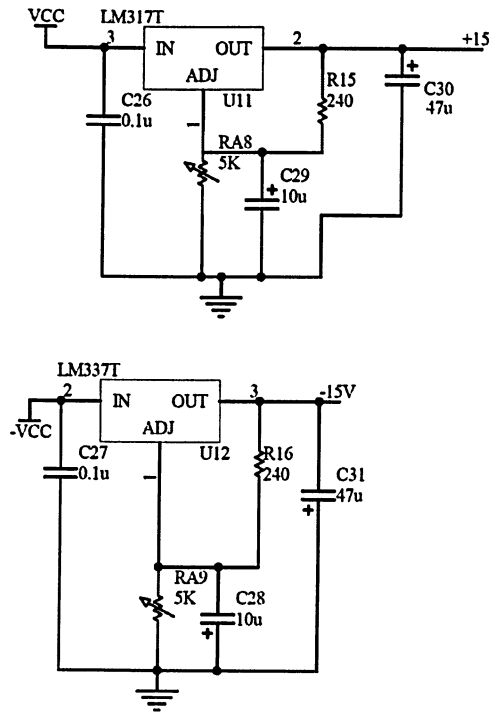


**Figure 2.24:** DC Power Supply for Subtractor

In this low noise DC power supply, a 3-terminal positive adjustable regulator, LM317 (National Semiconductor Co., LM317T), was used to provide +15 V DC, and a 3-terminal negative adjustable regulator, LM337 (National Semiconductor Co., LM337T) was used to provide -15 V DC.

#### 2.5.4 PCB Design

The PCB design followed two rules. One was that the layout of components should minimize the interference from AC to DC signal. The other was that the placement of the ground should separate the AC and DC circuit from each other, and shorten the route from the ground pins of components to the ground of the power supply.

Figure 2.25 shows the layout of the PCB. All AC signal circuit was placed on the lower part of the PCB, far away from the DC signal circuit, which was located on the





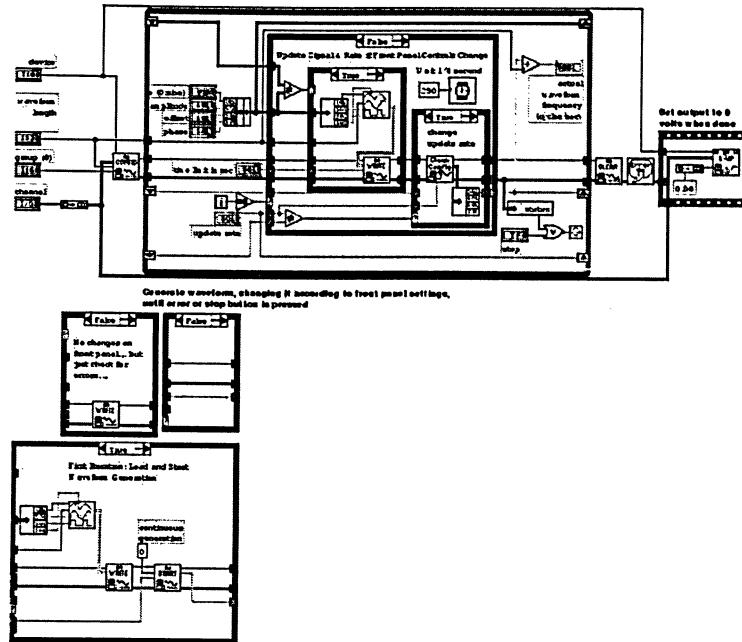


Figure 2.26: Labview diagram for the 20Hz control signal generator

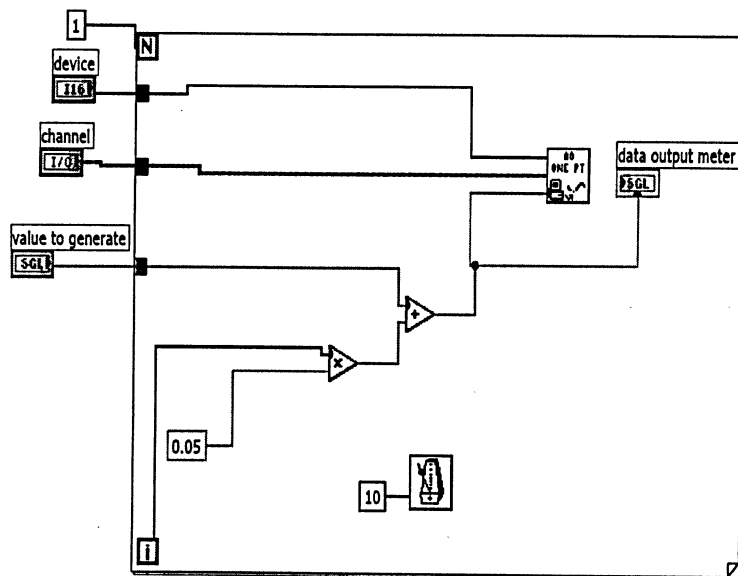


Figure 2.27: Labview diagram for the pulse signal generator

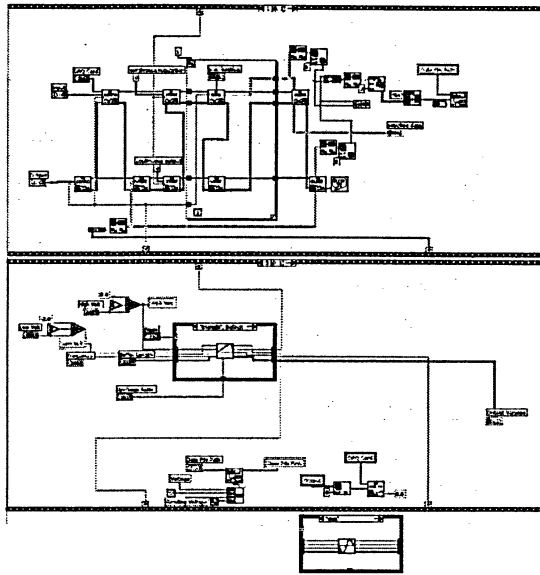


Figure 2.28: Labview diagram for the repeatability test

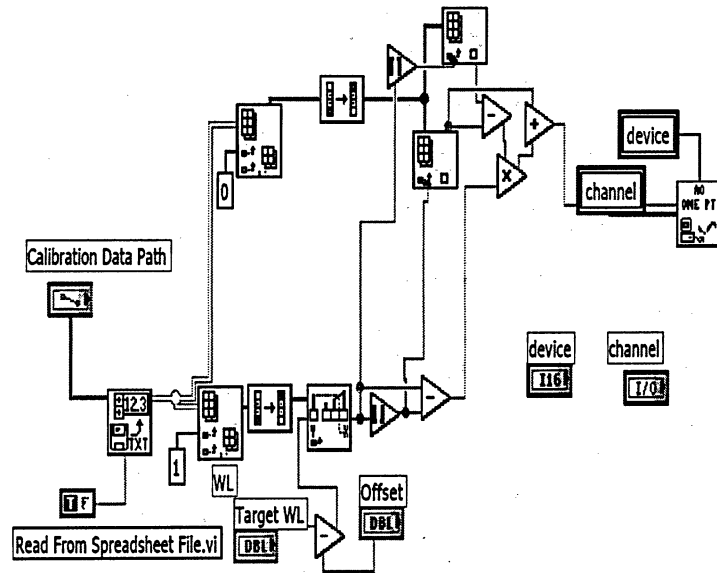
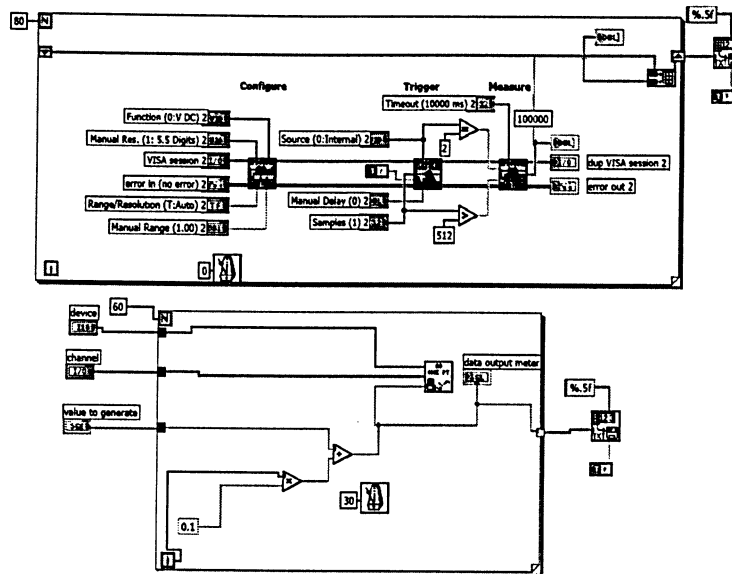


Figure 2.29: Labview diagram for the wavelength tuning



**Figure 2.30: Labview diagram for reading LVDT**

The program generated the control signal from DAQ card's output channel "output1", and read the LVDT output data from the DAQ card's input channel "input0". The control signal and the filter data were written to an Excel spreadsheet file before the program ended.

Figure 2.29 shows the Labview program for the filter's wavelength tuning test. The program read a spreadsheet file including the look-up table for tuning wavelength vs. the control signal, and sent the control signal, which matched the desired wavelength, to the subtractor circuit of the filter.

Figure 2.30 shows the Labview program for the filter calibration test and resolution test. In these tests, the program generated an increment step control signal from the DAQ card's output channel "output1", and read the LVDT output and wavelength meter from the input channel "input0" and "input1".

## 2.7 Filter Fabrication

### 2.7.1 Parts Machining

From Section 2.3.2, the minimum dimension of the actuator was the thickness of the hinges,  $170\text{ }\mu\text{m}$  and  $180\text{ }\mu\text{m}$ . A tight location and orientation tolerance of the actuator were required. Sitico Precision Machining Co. was contracted to machine the actuator, using electron discharge machining (EDM). The EDM can achieve  $10\text{ }\mu\text{m}$  accuracy while the conventional machining is limited to 25 to  $50\text{ }\mu\text{m}$  accuracy. The other parts were fabricated in a mechanical shop by traditional processes.

### 2.7.2 PCB Assembly

The PCB was fabricated with a milling machine in Dept. Electrical and Computer Engineering at Ryerson University. The machine cut routes on a copper clad laminates board. This is one of the easiest ways to fabricate the PCB. Because some of the PCB fabrication processes, e.g. plated through hole (PTH), Solder Resist Printing, and Solder Mask Over Copper, were not performed, the components were difficult to be soldered on the board, and all via needed to be sealed by solder before the assembly.

Two D-sub 9 connector were soldered on the PCB to connect the  $\pm 18\text{ V}$  DC power supply and a cable to a computer. One heat sink was attached on the top of AD698 to cool the chip.

The resistors R3 and R4 for the LVDT offset of output voltage swing were set as follows: R4 was  $81\text{ K}\Omega$ , R3 opened.

The phase lag/lead circuit showing in Figure 2.19 was designed to compensate for the phase shift between the primary winding and the secondary windings. Based on the circuit pre-test, the output of the LVDT secondary windings lagged behind the input of the the primary winding. Hence, the parameters of the phase lag/lead circuit were set as follows: C was  $150\text{ pF}||150\text{ pF}$ ,  $R_s$  was  $9.5\text{ k}\Omega$ , and  $R_T$  was  $25\text{ k}\Omega$ .

The following characteristics of the circuit were obtained from the circuit tests: resolution of  $1/25000$ , noise of  $25\text{ }\mu\text{V}_{p-p}$ , and drift of  $30\text{ ppm/C}$ . This circuit meets

the design requirements.

However, for high performance filter, the circuit with an extremely lower noise and drift is needed. Noise of this circuit mainly comes from the output of AD698. Increasing  $C_2$ ,  $C_3$ ,  $C_4$  and  $C_{SHUNT}$  could reduce the noise and improve the resolution of the filter. Nevertheless, it also reduces the bandwidth of the filter and decreases the stability of the filter. The drift of the circuit is from the AD698's thermal effect. AD698 generates amount of heat when it drives the LVDT. In this design, a heat sink was used to dissipate the heat on the surface of AD698. Adding a thermoelectric cooler (TEC) to control the surface temperature of AD698 would significantly reduce the drift.

### 2.7.3 FBG Guiding

Figure 2.31 shows the FBG guiding assembly. The length  $l_f$ , 42.4 mm, is the sum of

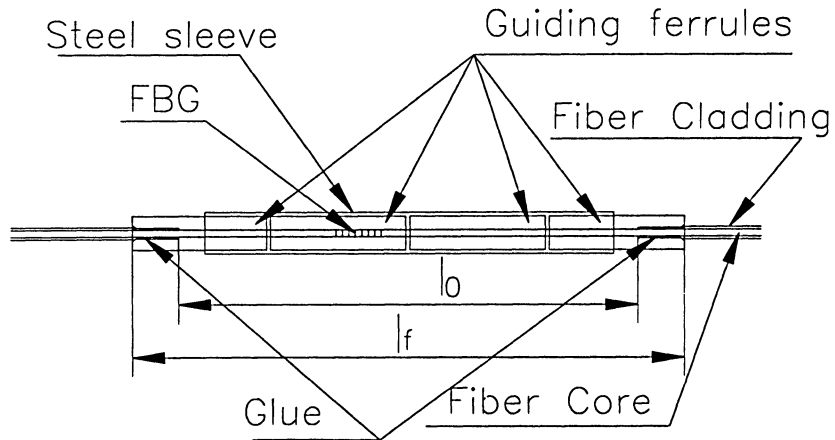


**Figure 2.31: FBG Guiding**

the length of four ferrules plus a gap for FBG compression. The length of the ferrule is 10.5 mm, and the gap should be equal to or slight longer than the length of the compressed fiber that was discussed in Section: 2.3.1,  $\Delta l_{ax} = 0.4$  mm. After applying the epoxy, the assembly was heated for the epoxy curing. The length  $l_0$  is the length

of optic fiber between two glued spots, i.e. the length of the glued fiber, which is a critical data used in the filter design (see Section: 2.3.1).  $l_0$  can be controlled by changing the heating process. Higher heating temperature makes  $l_0$  shorter. In this design, the cure temperature was set at 70 C, and the cure time, 2hrs. That gave  $l_0 = 24$  mm.

#### 2.7.4 Filter Assembly

Figure 2.32 shows the assembled mechanical parts of the filter. First, spacers and

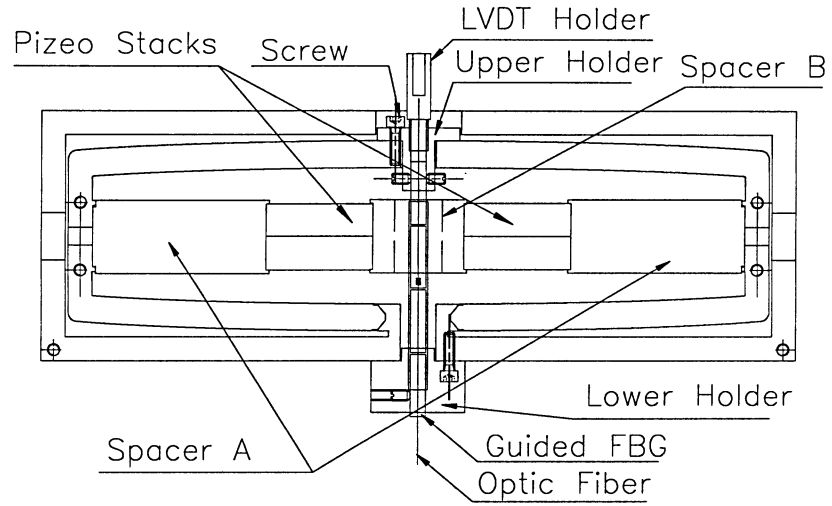


**Figure 2.32:** Filter assembly

piezo stacks were installed into the actuator. Then, the guided FBG was fixed on the lower holder by set screws. The lower holder and the guided FBG were fixed on the outside frame of the actuator by screws. Because one end of the guided FBG was fixed, any twist on the other end of the guided FBG could damage the FBG. After the upper holder was fixed on the frame, the LVDT holder was attached on to the upper holder. Four pre-load springs were installed on the actuator by screws.

# Chapter 3

## Filter Tests and Measurements

### 3.1 Introduction

THE following tests were set to verify the design and fabrication of the piezo drive tunable optic filter:

- Filter Calibration, to establish the correspondence between the tuning wavelength and the LVDT output.
- Closed Loop Tuning Speed, to measure the tuning speed of the filter using optical and electrical methods.
- Short Term and Long Term Drift, to test the filter's wavelength stability.
- Wavelength tuning Repeatability, to test the filter's dynamic stability.
- Tuning Resolution, to test the highest resolution of the filter in a required tuning range.
- Thermal Compensation Test, to verify the filter's wavelength stability as temperature varies.
- Filter Applications Test, to show the filter applications as a spectrometer and an optic channel switch, respectively.

## 3.2 Tests Setup

### 3.2.1 Optic Test Setup

Figure 3.1 shows the optic configuration for the following tests: filter calibration; long and short term drift; wavelength tuning repeatability; tuning resolution; thermal compensation. In these tests, a wavelength meter was used to accurately measure the wavelength of the filter. In the test of reflection spectra, an optical spectra analyzer (OSA) was used to record and analyze the spectrum of the filter.

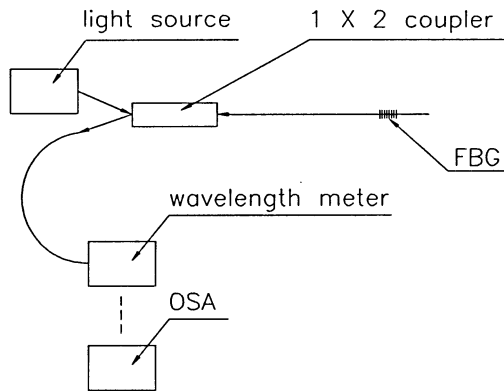


**Figure 3.1:** Optic system setup A

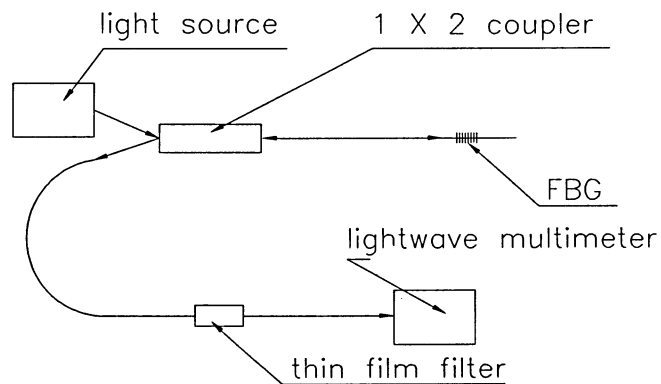


**Figure 3.2:** Optic system setup B

Figure 3.2 shows the optic configuration for tests: closed-loop tuning speed and filter scanning. A thin film filter and a lightwave multimeter were used in these tests



to detect the light power of the filter's output.

### 3.2.2 Instruments and Components Used In Tests

The instruments and components used in the tests are listed in Table 3.1:

Name	Manufactory	Model
Light Source	E-TEK	BLS
Wavelength Meter	HP	86120B
Lightwave multimeter	HP	8153A
Photo Detector (Optical Head)	HP	81521B
Optical Spectra Analyzer (OSA)	ANDO	AQ6331
Piezo Driver	General Photonics	PCD-001
Digital Phosphor Oscilloscope	Tektronix	TDS3032B
Multi-meter	HP	34401A
DC Power Supply	HP	E3630A
Hot Plate	Branstead	Hp46515
Thermoelectric Cooler	Leca	Ahp-301cp
Thin Film Filter	E-Tek	DWFI-07552
1X2 Coupler	E-Tek	SWBC2150PS210
DAQ Card	NI	6035E
3-Axis Precise Stage	Newport	M-561-T1LT-LH

**Table 3.1:** Instruments and devices

### 3.3 Tunable Filter Calibration

First, the LVDT was calibrated by establishing a relationship between the LVDT output and  $\Delta$  known displacement<sup>S/</sup>. A micrometer was used as a reference. Generally, the LVDT output was adjusted between 5 V to 6 V per millimeter in tests. This ratio varied depending on the relative location of the LVDT core and windings. Therefore, each time this relative location changed, the LVDT needs to be re-calibrated.

Then, a control voltage was sent from a computer to the subtractor. The filter responded to the control signal, and tuned to a wavelength measured by a wavelength meter. Filter calibration was carried out by recording the control signal , the LVDT

output, the reflected FBG wavelength, and the piezo driver output, establishing the relationships between the LVDT output and the tuning wavelength, and building the look-up table (Control signal vs. Tuning wavelength).

Figure 3.3 and Table 3.2 show the results of the filter calibration.

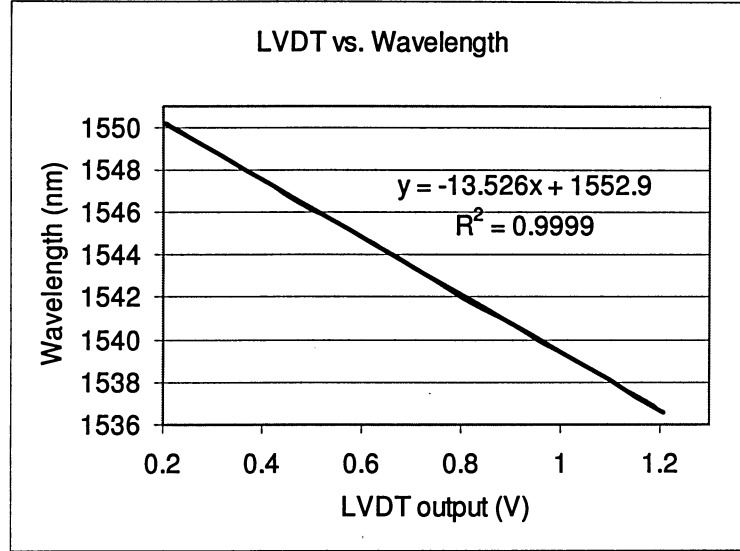


**Figure 3.3:** Filter Calibration (LVDT vs. Wavelength)

The tuning range of the filter, from 0 to 13.5 nm, was measured by adjusting the piezo driver output from -30 V to 150 V. It was shorter than the design goal of 20 nm. The reason was that the material for the actuator fabrication was not the same as the material used in the calculation. In the design, a cold drawn Invar 36 bar with the yield tensile strength of 679 MPa was used. In the fabrication, an annealed hot rolled Invar 36 bar with the yield tensile strength of 247 MPa was used. Repeating the ANSYS analysis in Section 2.3 with parameters of the annealed hot rolled Invar 36, M. of elasticity of 141 GPa and the yield tensile strength of 247 MPa, the maximum displacement of the frame in y-direction under the fatigue strength of material was 0.27 mm with the force of 9.8 N and the applied displacement in x-axis of 29  $\mu m$ . This result is less than that calculated in Section 2.3.1, 0.4 mm with the force of 14.5

Control Signal (V)	LVDT output (V)	Pz driver output (V)	Wavelength (nm)
-1.5	0.2011	-30	1550.208
-1	0.2059	-28.3	1550.214
-0.5	0.2573	-18.3	1549.501
0	0.312	-8.2	1548.733
0.5	0.3631	2.3	1547.975
1	0.4158	13.2	1547.29
1.5	0.4685	23.3	1546.508
2	0.5295	33.3	1545.771
2.5	0.5886	42.1	1545.051
3	0.6645	52.8	1544
3.5	0.733	62.7	1542.957
4	0.808	72.4	1541.912
4.5	0.879	82.2	1540.97
5	0.937	92.1	1540.192
5.5	0.9909	102	1539.511
6	1.0521	112.1	1538.74
6.5	1.1242	122.2	1537.73
7	1.1738	132.3	1537.1171
7.5	1.203	143.3	1536.65
7.8	1.208	149.5	1536.67

**Table 3.2:** Filter calibration

N and the applied displacement in x-axis of 20  $\mu m$ . From Equation 1.4, the maximum tuning range of the filter under the 0.27 mm compression was 13.55 nm. This was close to the test result, 13.5 nm. Though the design goal of the maximum tuning range was not obtained, the design process was proved.

### 3.4 Closed Loop Tuning Speed/Switching Time

The switching time of the filter was defined as the delay between the onset of the control signal and the detection of the fully reflected light (90% or -0.5 dB) at the required wavelength by a photo detector. A photo detector with a fast response time and a narrow band pass filter at 1541.39 nm with the -3 dB bandwidth of 0.3 nm were used for this test. In this arrangement, the detector would only "see" the light when the tunable filter was tuned from 1547.52 nm (start wavelength) to 1541.39 nm.

One feature of the system with a feedback control loop is when the system responds a pulse control signal, its output has a small variation. The same observation was made while testing. When responding to a pulse signal, the output wavelength of the filter showed a small variation before reaching a stable value. The wavelength error was defined as the amplitude of this wavelength variation, and the switching time was measured as a function of the wavelength error. Since the respond time of the Hp wavelength meter is in the order of 100 ms, it can not be used for the switching time measurement. The wavelength error was calculated from the output of the LVDT.

A 2-channel digital oscilloscope was used to record the pulse control signal and the LVDT output; the pulse control signal and the output of the photo detector. Figure 3.4 shows the traces of the control signal and the photo detector output. From this

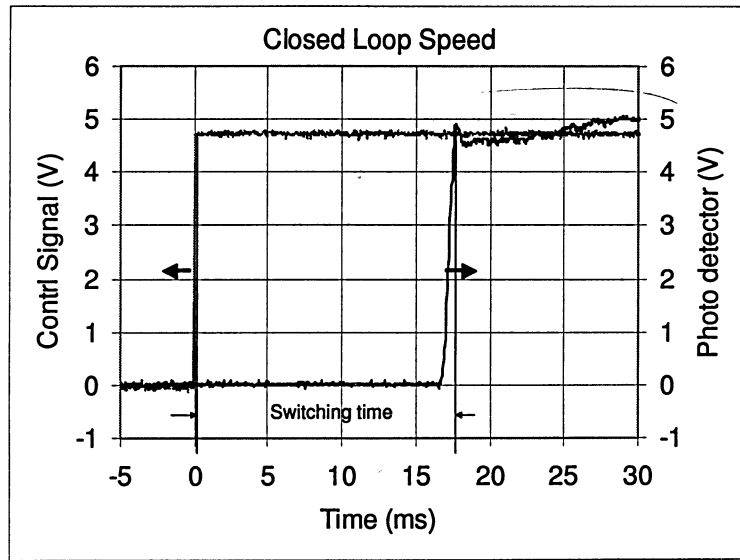


**Figure 3.4:** Control signal vs. Photo detector

figure, 17.3 ms switching time can be seen when a 90% light power was detected.

The wavelength error was calculated from Figure 3.5. When switching time was 17.3 ms, LVDT error,  $s$ , was 0.8%. The corresponding wavelength error was  $0.8\% \times \text{tuning range}(6.13 \text{ nm}) = 0.049 \text{ nm}$ . Therefore, the switching time of this filter

was 17.3 ms for the tuning range of 6.13 nm with a 49 pm wavelength error.

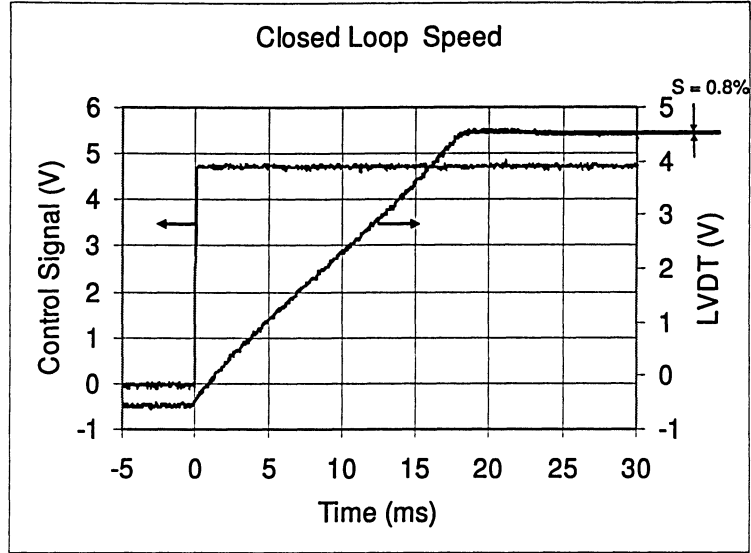


**Figure 3.5:** Control signal vs. LVDT output

The following factors would affect the switching time: piezo stacks and the piezo driver, the feedback control loop, the NI DAQ card, the actuator, and the LVDT.

From the LDVT and the piezo driver's specification datasheets, the delay of the LVDT and the piezo driver are less than 1 ms and 0.03 ms, and the responds times of the actuator, the NI DAQ card, and the piezo stack are less than 1  $\mu s$  [39][22][23]. Therefore, the 17.3 ms filter switching time was mainly from the feed back loop.

The feed back control circuit was used in the filter tuning control for higher accuracy and stability. However, the feed back control loop restricted the system's dynamic responds, i.e. the tuning speed. If the applications require a lower accuracy, the feed back control can be changed to achieve a higher filter tuning speed.

The tuning speed test was repeated ten times to determine the variation of the switching time, and a range between 17 ms to 17.4 ms was found for the switching time as shown in Figure 3.6.

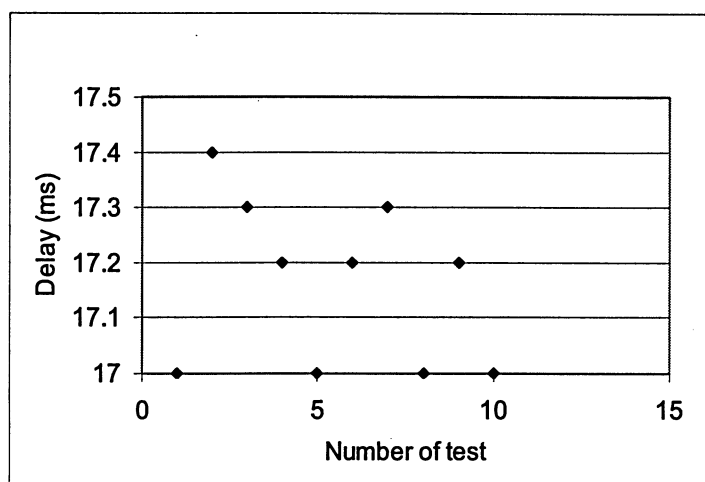


Figure 3.6: Switching time variation

### 3.5 Short and Long Term Drift

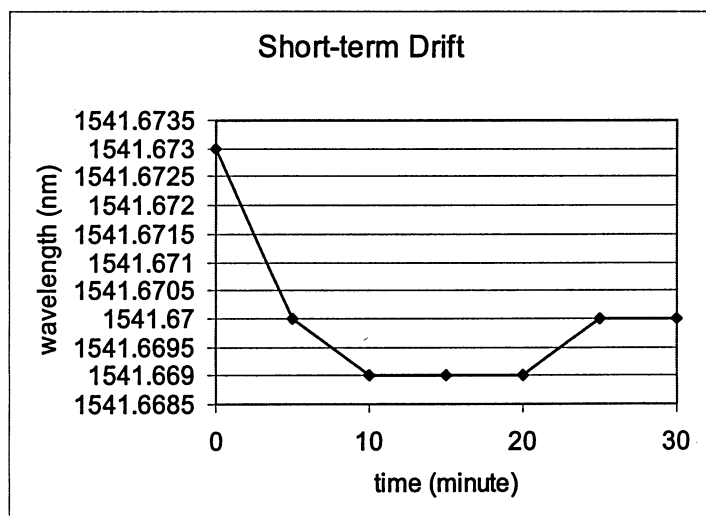
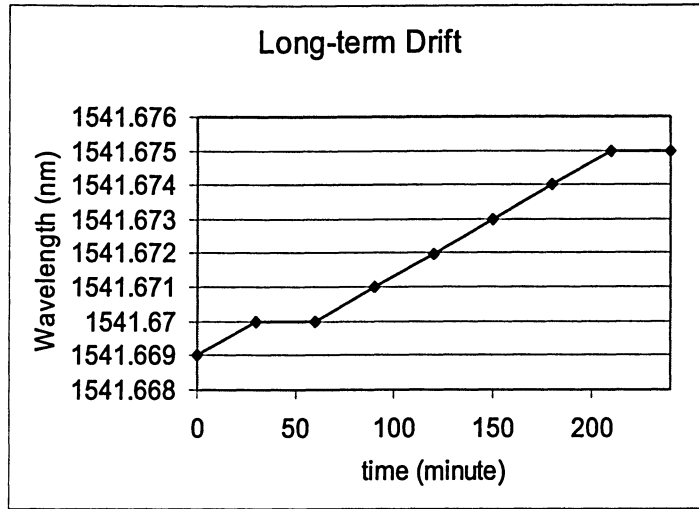


Figure 3.7: Short term drift

The filter short-term drift were tested by recording the FBG's output wavelength every 5 minutes for 30 minutes. It was less than 4 pm. Figure 3.7 shows the filter short-term drift of 4 pm.



**Figure 3.8:** Long term drift

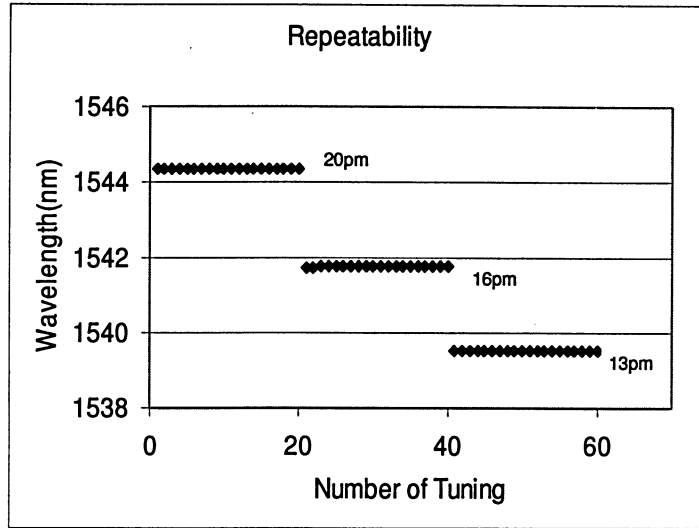
The filter long-term drift were tested by recording the FBG's output wavelength every 30 minutes for eight hours. It was less than 6 pm. Figure 3.8 shows the filter long-term drift of 6 pm.

### 3.6 Wavelength tuning Repeatability

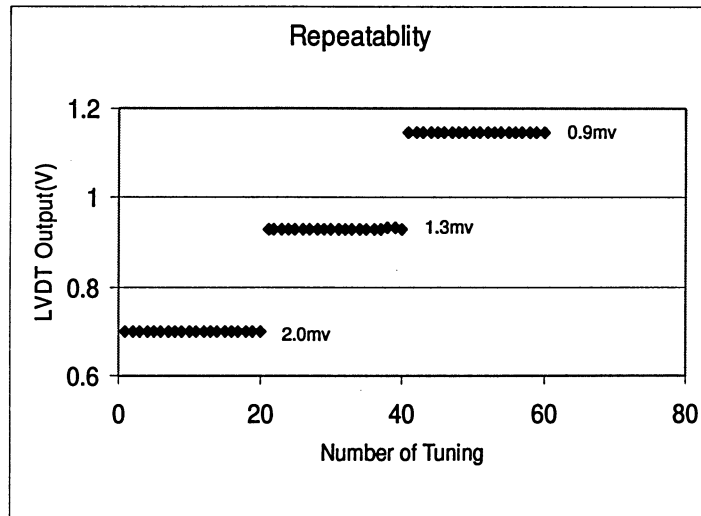
In order to test the filter's tuning repeatability, the tuning of the filter from the start wavelength to three different wavelengths were repeated for 20 times. The tuned wavelength reading from the wavelength meter and the corresponding output of LVDT were recorded. The variation of the wavelength, the tunable filter's tuning repeatability, were determined from those recorded wavelengths.

Figure 3.9 shows tuned wavelengths at three different tuning ranges. Figure 3.10 shows the corresponding LVDT output.

The optical repeatability variation of the filter was 20 pm for the 3 nm tuning (from 1547 nm to 1544 nm), 16 pm for the 6 nm tuning (from 1547 nm to 1541 nm), and 13 pm for the 8 nm tuning (from 1547 nm to 1539 nm). The corresponding electronic repeatability variation of the filter are: 2 mv for the 3 nm tuning, 1.3 mv for the 6 nm tuning, and 0.9 mv for the 8 nm tuning, respectively.



**Figure 3.9:** Tuning repeatability of the filter tuned 20 times to three different wavelengths



**Figure 3.10:** The corresponding LVDT measurements when the filter were tuned to three different wavelengths for 20 times

The repeatability variation reduced as the tuning range increased. The reason could be the stiffness of the frame increased with the increase of displacement. This indicates that applying a higher pre-load could further improve the filter's repeatability.



bility.

### 3.7 Tuning Resolution

The tuning resolution of the actuator was defined as the minimum repeatable displacement increment that an actuator can generate under an applied control signal increment.

The tuning resolution of the filter was defined as the minimum repeatable wavelength increment that the filter can generate under an applied control signal increment.

In the previous actuator tests [27], the tuning resolution of the actuator was  $\pm 20\text{nm}$  within 0.9 mm tuning range, or  $1/22500$ , with  $F=0$ .

Figure 3.11 shows the tuning resolution of the tunable filter.

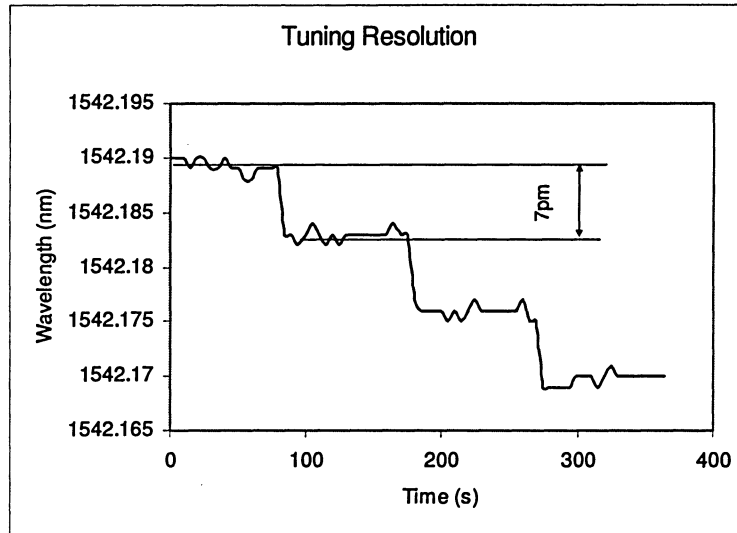


**Figure 3.11:** Resolution of the filter

The control signal with an incremental step, 4 mv, was applied from a computer. The wavelength shift generated by the control signal was read from a wavelength

meter. The minimum repeated wavelength shift of the filter, 7 pm in a tuning range of 8 nm, was obtained. This resolution is currently limited by the 12bit D/A in the NI DAQ card.

Figure 3.12 shows the corresponding output of the LVDT during the resolution test. The resolution of the LVDT output was about 580  $\mu V$ . The corresponding displacement was 120 nm. From the calculation in Section 2.3.1, the 120 nm compression generated wavelength shift of FBG, 6.3 pm. This was close to the resolution reading from Figure 3.11.

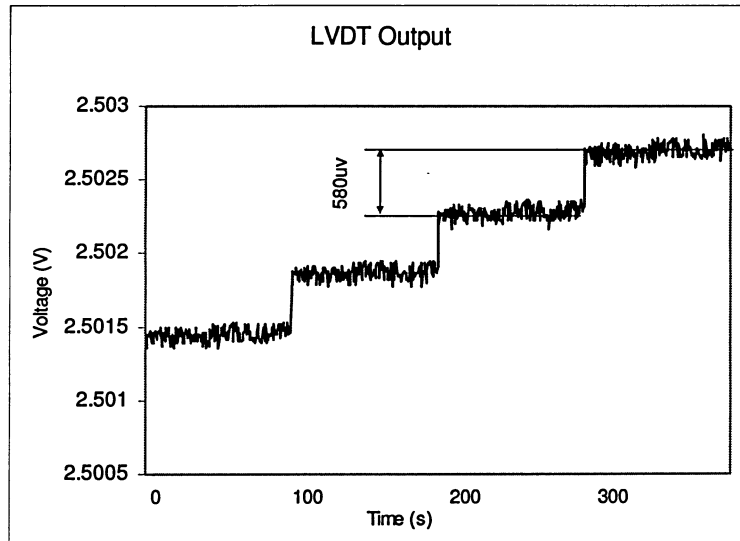


**Figure 3.12:** Corresponding output of the LVDT

The resolution of the filter was affected by the pre-load and the frictions among the sleeve, ferrules, and the optic fiber. A large pre-load will improve the filter's resolution. If the friction between fiber and its guiding system can be reduced, a higher resolution can be obtained. However, the friction can't be eliminated, because the ferrules and the sleeve need fraction to hold the optic fiber, to keep the fiber from micro-bends, and to maintain the concentricity between optic fiber guiding parts.

In addition, the accuracy of manufacture and assembly of the filter components

may also limit the resolution of the filter.

### 3.8 Thermal Compensation Test

During this test, the filter was set on a hot plate (Branstead, Hp46515) or on a thermoelectric cooler (TEC)(Leca, Ahp-301cp), and was tuned to a certain wavelength. The wavelength of the filter was measured at different temperatures to verify its thermal stability. The hot plate and the TEC maintain the temperature on the actuator with an error of  $\pm 1$  C.

First, the filter was put on the hot plate, and the hot plate temperature was set to 20 C, 30 C, and 40 C. The filter's wavelength was recorded at every temperature after the temperature on the actuator reached equilibrium,  $\pm 1$  C. Then, the actuator was put on the TEC, and the temperature was set to 10 C. The filter's wavelength was recorded after the temperature reached equilibrium.

The thermal compensations with five different spacers and FBGs were tested. Table 3.3 shows the test results.

	$l_0(\text{mm})$	Spacer A, $l_A(\text{mm})$	Spacer B, $l_B(\text{mm})$	$\Delta \lambda/T(\text{pm/C})$
Case I		SS304, 32.57	SS304, 4.33	-124
Case II	23.9	Invar 36, 32.57	SS304, 4.33	+25.1
Case III	28.07	Invar 36, 29.13	SS304, 7.73	+3.7
Case IV	24.12	Invar 36, 29.12	SS304, 7.73	+2.8
Case V	23.88	Invar 36, 29.07	SS304, 7.84	+1.5

**Table 3.3:** The results of thermal tests with different spacers

In this table,  $l_A$  and  $l_B$  are the length of the spacer A and B, respectively.  $l_0$  is the length of the guided fiber. SS304 is Type 304 stainless steel.  $\Delta \lambda/T$  is the average wavelength change per degree of the temperature.

Figure 3.13 shows the thermal test result in Case V at two wavelengths, 1544 nm and 1538.8 nm, respectively.

The wavelength stability, 1.5 pm/C, was obtained in this test. It meets the design requirement. This value is comparable to the wavelength stability of thin-film based

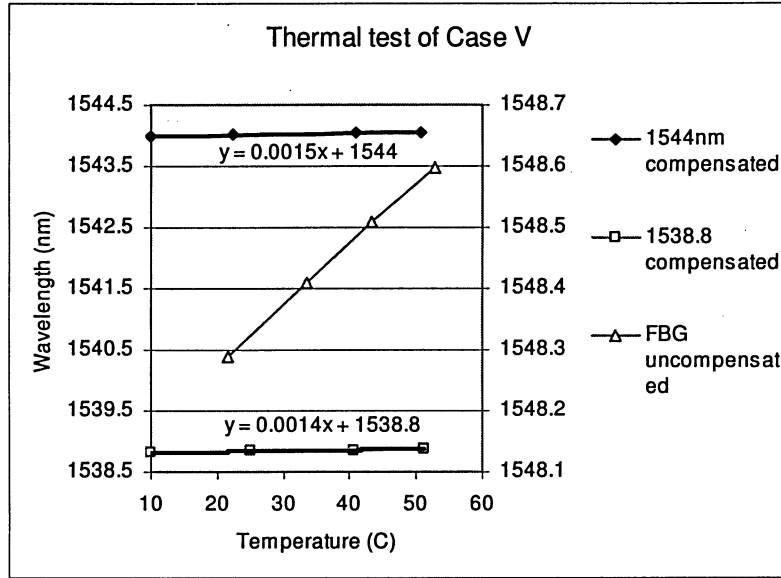


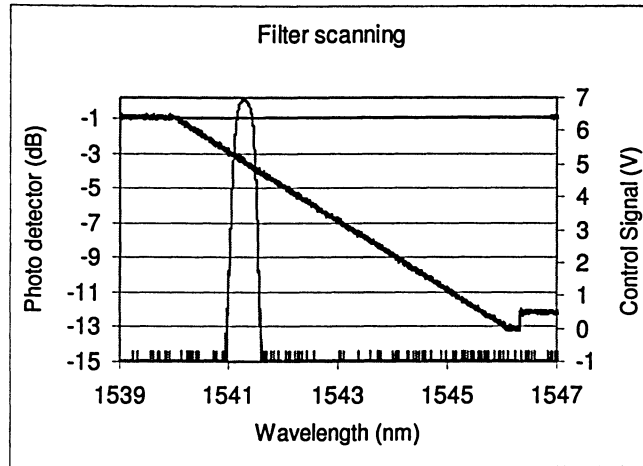
**Figure 3.13:** Result of the thermal test, Case V

WDM filters on market, i.e. 1 ~ 2 pm/C.

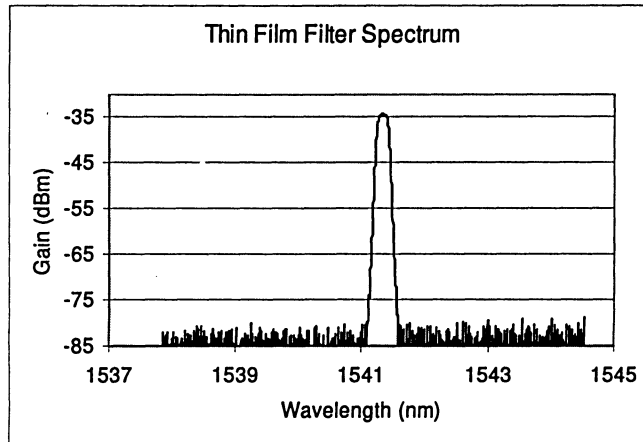
The CTE values of piezo and Invar 36, which were used in the design, affected the calculation of the thermal compensation. From different sources, the CTE of piezo changed from -3 ppm/C to -6 ppm/C. In calculation, the CTE of piezo stack was determined to be -4.5 ppm/C based on the test data. The CTE of Invar 36 changes from 0.8 to 1.6 ppm/C depends on the suppliers. 0.96 ppm/C were used as the CTE of the Invae36 in the thermal compensation calculation.

### 3.9 Filter Applications Test

An narrow band tunable FBG can be used to scan spectral profiles of the other types of filters. In this test, the tunable filter was scanned over the spectrum of a standard 100 GHz DWDM thin film filter (centred at 1541.39 nm with 0.3 nm -3dB bandwidth). Figure 3.14(a) shows the spectrum of the DWDM filter measured with the tunable filter. Figure 3.14(b) shows the spectrum of the thin film filter measured with an OSA. Comparing these two plots, it can be seen that these spectral profiles



(a)



(b)

**Figure 3.14:** (a)The Spectra of Thin Film Filter measured by the tunable filter (b)Filter measured by an OSA

are almost identical.

The reflection spectra of the FBG at different center wavelengths in a tuning process are showed in Figure 3.15 with the piezo driver output changed from 0 V to 120 V. From the first peak in the right in Figure 3.15 to the last peak in the left, the

piezo driver output(V) are at: 0, 20.2, 30.1, 40.1, 50.3, 60, 70, 80, 90.5, 100, 110.5, and 120.2, respectively. It simulated the application of the tunable filter as a channel switch in an optic communication system with the channel spacing of 0.8 nm(100 GHz). The filter isolation band remains larger than 35 dB, and there is almost no change in the spectra shape.

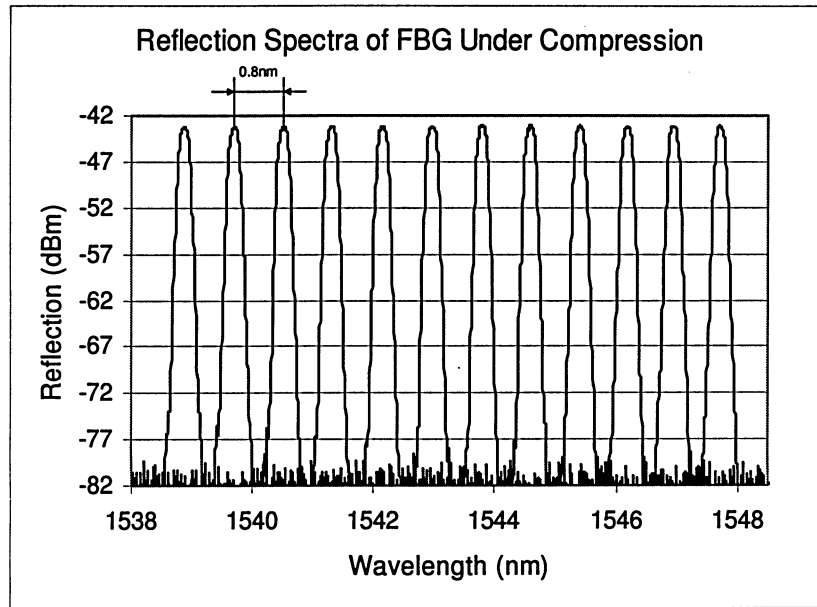


**Figure 3.15:** FBG Reflection Spectra

# Chapter 4

## Conclusions

### 4.1 Summary of thesis

**M**Y objective is to design an optic tunable filter with a fast tuning speed, a high tuning resolution, a stable thermal behavior, and a high reliability. In this thesis, a piezo drive optic tunable filter based on a fiber Bragg grating was described. The proposed filter was constructed and tested. The results were presented and discussed.

Two piezo stacks with a 40  $\mu\text{m}$  total stroke were used as the displacement generator, and an ellipse shape actuator was designed to magnify the piezo stroke to 0.4 mm under a reaction force of 14.5 N. The actuator was made of Invar 36 to minimize the thermal induced wavelength drift. An LVDT was used to monitor the displacement of the actuator and to provide the feedback control loop for the wavelength tuning of the filter. The feedback control loop provided the higher resolution and better stability of the filter. Labview programming and NI DAQ card were used to perform the wavelength tuning of the filter.

Two spacers with different CTEs were designed to compensate for the thermal effect of the FBG and the actuator.

Noise control and the precision of the control circuit were analyzed in the electronic design. Precision, Zero-Drift operational amplifier, LTC1150, was used to build the subtractor. A low noise DC power supply was designed to separate the power supply for AC and DC circuit. In the PCB design, AC and DC circuit were separately placed

to minimize AC noise.

Table 4.1 shows the achieved performances.

Closed Loop Switch time	17.3 ms
Resolution	7 pm
Maximum Tuning range	13.5 nm
Repeatability	26 pm
Thermal Compensation	1.5 pm/C

**Table 4.1:** Characteristics of the tunable filter

Based on the implementation and the results, some major conclusions can be drawn as follows:

- The flexible hinges of the elliptic shaped structure significantly expand the displacement of up to 30 times without load. However, the displacement reduces as the load increases. At a load of 14.5 N, the displacement of magnification of 4.5 is obtained. FEA software, ANSYS, is effective tool in the calculation of the structure with sufficient accuracy.
- Carefully designing and fabricating the thermal compensation spacers can reduce the thermal-induced wavelength drift of the filter to almost zero. This thermal compensation design is effective and relatively easy to be implemented.
- Mechanical precision is one of the key factors for designing this kind of device. If the tolerance of the upper and lower holders could be control under  $5\ \mu m$ , the whole performance of the filter would be higher. However, the fabrication cost could be significantly higher.

## 4.2 Contributions

In this thesis, an FBG based optic tunable filter was investigated using two piezo stacks as the displacement generator , and an ellipse shape actuator with 16 flexible



hinges as the displacement expander. This design realized a high performance, low cost, and compact optic tunable filter.

The switching time of 17.3 ms was achieved, this is much shorter than the 50 ms switching time reported before [23].

The resolution of 7 pm was obtained. This is the highest resolution of this kind of tunable filter reported so far.

As low as 1.5 pm/C thermal-induced wavelength drift was achieved.

In this design, the FEA method was used to design the filter and its thermal compensation. It was proved to be simple and economical.

With Labview programs and a NI DAQ card, the filter could be easily operated , and its features could be changed to meet different applications.

As the test results show, the design specifications for this filter have been achieved, except the tuning range. It is shorter than the design goal due to the different materials used in the design and in the fabrication.

This is the first time, to my knowledge, that a tunable fiber optic filters with all those features has been designed and fabricated.

## **4.3 Future research**

In this section, several proposals are presented, which will further enhance the performance of the filter.

### **4.3.1 Displacement Expanders with Large Stroke Gain Under a Force Load**

From the above described optic tunable fiber design, a 13.5 nm wavelength tuning range has been obtained. However, the tuning range of over 20 nm would be more useful in many applications. In this section, several stroke expanders are proposed that will extend the tuning range to more than 20 nm.

As mentioned in Section 3.3, the actuator was made of an annealed hot rolled Invar 36 bar, though a cold drawn Invar 36 bar was used in its design. The yield

tensile strength of the annealed hot rolled Invar 36 is 274 MPa, and that of the cold drawn Invar 36 is 679 MPa. If a cold drawn Invar 36 is used to fabricate the actuator, the allowed fatigue strength will increase from 1110  $\mu\epsilon$  of the annealed hot rolled Invar 36 to 2752  $\mu\epsilon$ . Thus, the maximum tuning range will increase from 13.5 nm to 29 nm. The disadvantage of the material change is the higher CTE of the cold drawn Invar 36 (shown in Table 4.2). This will change the thermal responds of the filter, and the thermal compensation spacers need to be re-calculated . Table 4.2 shows the comparison of some parameters of two filters made of these two Invar 36.

	Annealed Hot Rolled	Cold Drawn
Tensile strength, yield(Mpa)	274	679
Allowed Max. Strain ( $\mu\epsilon$ )	1110	2400
Max. Tuning Range (nm)	13.5	29
CTE (ppm/C)	0.96	1.3

**Table 4.2:** Filter made of the annealed hot rolled Invar 36 vs. Filter made of the cold drawn Invar 36

The second way to achieve a larger displacement and a stronger force is to change the material of the hinges. The hinges made of Invar 36 with a limited yield strength can not take a high strain. Changing the hinge material from Invar 36 to other metals with a higher yield strength, e.g. Titanium alloy, is possible for a larger stroke amplification and a stronger force.

Titanium is 30% stronger and nearly 50% lighter than steel. Titanium can be alloyed with aluminum, manganese, iron, molybdenum and other metals to increase strength and high temperatures endurance, and to reduce the weight. Titanium's high corrosion resistance is also a valuable characteristic. When exposed to the atmosphere, titanium forms a tight, tenacious oxide film that resists corrosive environments. Titanium is being increasingly utilized for medical applications due to its lightweight, its strength, and its hypoallergenic properties since titanium is nickel free. Titanium products are becoming increasingly utilized in other industries as well, from petrochemical applications to sporting goods.

In this Ti-hinge actuator design, Titanium Ti-6Al-4V (Ti-6-4 or ASTM Grade 5

Titanium) was selected to fabricate the hinges of the actuator. Table 4.3 lists the properties of the Ti grade 5 and compares them with the same properties of other metals.

Material	M. of Elasticity (GPa)	$\alpha$ ,CTE (ppm/C)	Poisson's Ratio	Shear M.(GPa)	Tensile S. Yield(MPa)
Type 430 Stainless Steel	200	10.4, 0-100C	0.29	86	441
Type 304 Stainless Steel	200	17.3, 0-100C	0.29	86	205
Invar 36 (annealed)	141	0.96	0.3	60	274
Invar 36 (cold drawn)	148	1.3	0.3	60	679
Titanium grade 5	114	8.6	0.423	44	1070

**Table 4.3:** A comparison of material properties

Two model of the Ti-hinge actuator was built with ANSYS. One used a double Ti hinges structure in a Invar 36 frame and the other with a single hinge structure in the Invar 36 frame. Figure 4.1 shows the model of the double-Ti-hinge actuator and Figure 4.2 shows the model of the single-Ti-hinge actuator. In these two models, the Invar 36 frame and Titanium hinges can be spot- welded or seam-welded together by Laser.

This hybrid structure used the lower CTE property of Invar 36 for easier thermal compensation and the high strength of Titanium alloy to generate a large displacement amplification at a high load. Table 4.4 lists the ANSYS results of those two models, Model 2 (the double-Ti-hinge actuator ) and Model 3 (the single-Ti-hinge actuator). The model of the whole Invar 36 actuator (Model 1 in Table 4.4) was also listed as a reference.

From the ANSYS results, it can be seen that both the single-Ti-hinge actuator and the double-Ti-hinge actuator meet the requirements of over 20nm FBG tuning range. The single-Ti-hinge actuator has the higher performance than that with double-Ti-

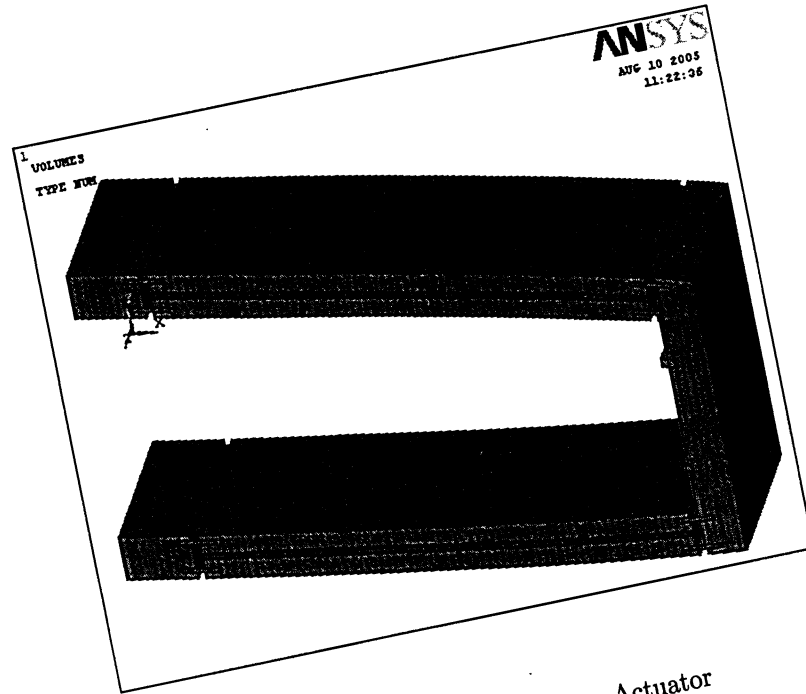


Figure 4.1: Double-Ti-Hinge Actuator

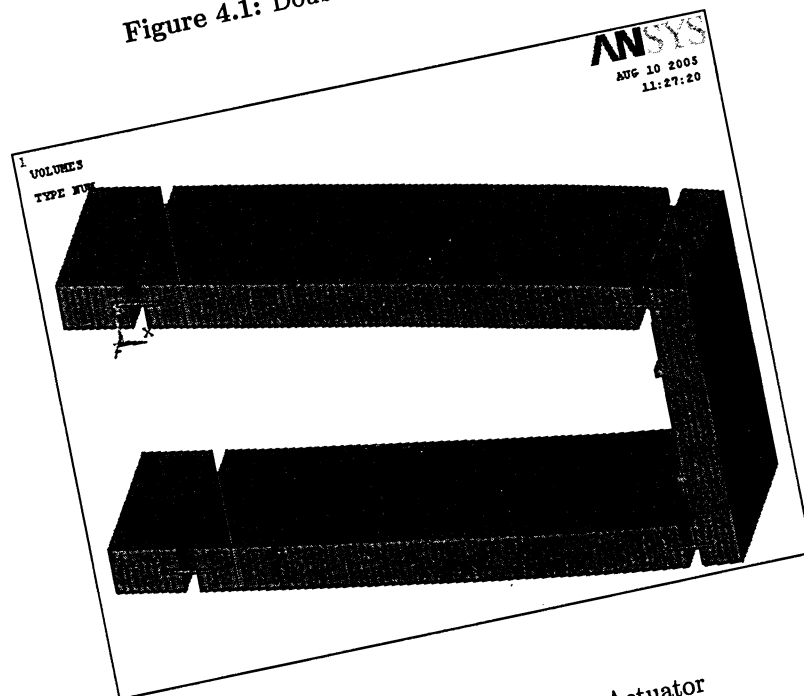


Figure 4.2: Single-Ti-Hinge Actuator

	Hinge Thickness (mm)	Hinge Length h (mm)	$\Delta x = 20 \mu m$ F = 0			$\Delta x = 20 \mu m$ F = 14.5N			Thermal Expansion (10 <sup>-6</sup> m/10C)	
			$\Delta y$ (mm)	Stroke Gain	Max. Strain ( $\mu \epsilon$ )	$\Delta y$ (mm)	Stroke Gain	Max. Strain ( $\mu \epsilon$ )	x-axis	y-axis
Model 1	0.18	0.59 ~0.9	1.234	30.85	-1371	0.4	10	-1090	0.49	0.30
Model 2	0.406	0.75	0.8	20	-1748	0.523	13.1	-1028	0.87	0.85
Model 3	0.406	1.4	1.073	26.8	-1489	0.608	15.2	-550	0.96	0.96

**Table 4.4:** Ansys results of the actuator with Ti hinges

hinge, and is relatively easier to be fabricated.

#### 4.3.2 Rebuild ANSYS Model For Thermal Compensation Calculation

In the ANSYS calculation, the guided FBG assembly was not included in the ANSYS model due to the difficulty of the model building and meshing. The calculation of FBG's thermal effect was separated from the actuator. Integrating these two parts in one ANSYS model will improve the precision of the calculation, thus better thermal compensation.

### **4.3.3 Improve The AD698's Heat Dissipation**

The error of the circuit mainly comes from the thermal drift of AD689. Generally, every IC has a zero or a minimum drift at a certain temperature. Using a thermoelectric cooler (TEC) to stabilize the temperature of AD689 to its zero drift temperature will minimize the circuit error, and finally improve the filter's performance.

### **4.3.4 Re-design The Fiber Guiding System**

In the assembly of the guided FBG and its installation, the process involves the handling of the bare fiber, a piece of glass with a diameter of  $125\mu m$ . Poor fiber guiding also increases the risk of fiber breakage in the filter's applications. New design of the fiber guiding system and holders are needed to provide the better protection for the FBG.

The reduction of the friction among fiber, sleeve and holders, such as adding lubricant, will help protect the FBG, and improve the filter's resolution.

### **4.3.5 Expand The Application of The Tunable Filter**

The optic tunable filters are commonly used in fiber optic communication, as described Chapter 1 of this thesis. However, their applications are not limited to this area. They can be used in many other areas. For example, in Optic Sensing and Communication Lab at Ryerson University, researchers are studying the application of the sub-picometer fiber optic bandpass filter in wireless communication. The optic tunable filter can be easily used in their project, to build a sub-picometer tunable filter for wireless communication. The optic tunable filter can also be used in high-resolution spectroscopy, such as vibrational-rotational spectrum of gases.

# Bibliography

- [1] Domash, L.; Ming Wu; Nemchuk, N.; Ma, E.; "Tunable and switchable multiple-cavity thin film filters" Journal of Lightwave Technology, Journal of Volume 22, Issue 1, pp.126 - 135, Jan 2004
- [2] H Toba, K Oda, K Nakamshi, N Shbata, K Nosu, N Takato, and respectively M Fukuda, "A 100-channel optical FDM transmission / distribution at 622 Mbp/s over 50 km," Journal of Lightwave Technology, vol. 8, pp. 1396-1401, Sept 1990
- [3] A. Frenkel and C. Lin, "Inline tunable etalon filter for optical channel selection in high density wavelength division multiplexed fiber systems," Electronic Letter, vol. 24, pp. 159-161, Feb. 1988
- [4] Y. Fujii and J. Minowa, "Wavelength tunability of electro-optically tuned Fabry-Perot filters," Application Optic, vol. 30, pp. 1017-1018, Mar.1991
- [5] K Hirabayashi, H Tsuda, and T Kurokawa, "Tunable liquid-crystal Fabry-Perot interferometer filter for wavelength-division multiplexing communication systems," Journal of Lightwave Technology, vol. 11, pp 2033-2043, Dec 1993
- [6] D.A.Smith and J J Johnson, "Sidelobe suppression in an acoust-optic filter with a raised-cosine interaction strength," Appl Phys. Letter, vol. 61, pp. 1025-1027, Aug 1992
- [7] T Numai, "1.5 pm phase-shift-controlled distributed feedback wavelength tunable optical filter," IEEE Quantum Electronic, vol. 28, pp.1513-1519, June 1992

- [8] P. Tang, O. Eknayan, and H. F. Taylor, "Rapidly tunable polarization independent optical add-drop multiplexer in Ti : LiNbO<sub>3</sub>," *Electronic Letter*, vol. 38, pp. 242-244, 2002.
- [9] M. C. Larson, B. Pezeshki, and J. S. Harris, Jr, "Vertical coupled-cavity micro interferometer on GaAs with deformable membrane top mirror," *IEEE Photonic Technology Letter*, vol. 7, pp. 382-384, 1995
- [10] M. S.Wu, E. C. Vail, G. S. Li, W. Yuen, and C. J. Chang-Hasnain, "GaAs micromachined widely tunable Fabry-Perot filter," *Electron. Letter*, vol. 31, pp. 1671-1672, 1995
- [11] C. Chang-Hasnain, "Widely tunable VCSEL using MEMS technology," *Proc. LEOS 2000, MF1*, pp. 54-55, 2000
- [12] Hill, K.O., Meltz, G., "Fiber Bragg grating technology fundamentals and overview", *Journal of Lightwave Technology*, Journal of Volume 15, Issue 8, pp. 1263 - 1276, Aug. 1997
- [13] H. G. Limberger, N. Hong Ky, D. M. Costantini, R. P. Salathe, C. A. P. Muller, and C. R. Fox, "Efficient active Bragg grating tunable filters," in *Proc. OFS '97, OSA Tech. Dig. Series, OSA Topical Meeting, Williamsburg, USA, 1997*
- [14] G. A. Ball and W. W. Morey, "Tunable Bragg grating fiber filters and their applications," in *Proc. CLEO'97, Baltimore, MD*, pp. 108-109, 1997
- [15] M. M. Ohn, A. T. Alavie, R. Maaskant, M. G. Xu, F. Bilodeau, and K. O. Hill, "Dispersion variable fiber Bragg grating using a piezoelectric stack," *Electronic Letter*, vol. 32, pp. 2000-2001, 1996
- [16] A. Iocco, H. G. Limberger, and R. P. Salathe, "Bragg grating fast tunable filter," *Electronic Letter*, vol. 33, pp. 2147-2148, 1997
- [17] S. M. Melle, K. Liu, and R. M. Measures, "Practical fiber-optic Bragg grating strain gauge system", *Appl. Opt.*, vol. 32, no. 19, pp. 3601-3609, 1993



- [18] Andreas Othonos and Kyriacos Kalli, "Fiber Bragg grating,Fundamental and Applications in Telecommunications and Sensing", Boston, MA, Artech House, 1999
- [19] Alessandro Iocco, Hans Georg Limberger,et al. "Bragg Grating Fast Tunable Filter for Wavelength Division Multiplexing", Journal of Lightwave technology , vol.17, no. 7, pp.1217 - 1221, July 1999
- [20] N. Mohammad, W. Szyszkowski, W. J. Zhang, E. I. Haddad, J. Zou, W. Jamroz, and R. Kruzelecky, "Analysis and Development of a Tunable Fiber Bragg Grating Filter Based on Axial Tension/Compression" Journal of Lightwave Technology, Volume 22, Issue 8, pp:2001 - 2013, Aug. 2004
- [21] Kenji Uchino, "Piezoelectric Actuator and Ultrasonic Motors", Norwell, MA, Kluwer Academic Publishers, 1997
- [22] APC International Ltd., "Piezo-Mechanics: An Introduction", PA, 2003
- [23] Kenichro Takahashi, Mituaki Tamura, et al.,"Reconfigurable optical add/drop multiplexer using passive temperature-compensated wavelength tunbale fiber Gragg grating", Sumitomo Electric Industries, LTD. 1, Taya Sakae, Yokohama, Kanagawa, Japan, 2000
- [24] Colin Woolger,"Invar - Nickel Iron Alloy", Materials World, Vol. No. pp. 332-33, June 1996
- [25] S. Dierks, "Invar36" ESPI Corp Inc., Ashland, September 1991
- [26] F. Claeysen, N. Lhermet, R. Le Letty, F. Braillet, M. Debarnot, M. F. Six, F. Thomin, "Piezoelectric Actuators and Motors Based on Shell Structure", Smart Structure and Materials 2000, SPIE Vol.3991(2000), pp.202-209, 2000
- [27] W. Zu, X. J. Gu, "Amplified piezoelectric actuator with fine linear resolution", Photonic North 2004, Ottawa, CANADA, SPIE Vol.5577, pp.373-380, 2004

- [28] F.Claeyssen, N. Lhemet, R. Le Letty, F. Barillot, M. Debarnot, M.F. Six, G. Thomin, M.Privat and P. Bouchilloux, in Smart "Structure and Materials 2000", Proceedings of SPIE Vol. 3991, p202-209, 2000.
- [29] G.Meltz, "Overview of fiber grating-base sensors", in Destributed and Multiplexed Fiber Optic Sensors VI,Denver, Cololador.Proc.SPIE Vol. 2838, pp.2-21, 1996
- [30] *AD698 - Universal LVDT Signal Conditioner Datasheets*,Analog Devices, Inc, REV B, 1995
- [31]  *$\pm 15$  V Zero-Drift, Precise Operational Amplifier with Internal Capacitors*, Linear Technology Inc, Milpitas, CA, 1991
- [32] Y. Zhu, C. Lu, B. M. Lacquet, P. L. Swart, and S. J. Spammer, "Wavelength-tunable add/drop multiplexer for dense wavelength division multiplexing using long-period gratings and fiber stretchers," *Optical Communication*, vol. 208, pp. 337-344, 2002
- [33] Ramachandran, S. Ghalmi, S. Chandrasekhar, I. Ryazansky, M. F. Yan, F. V. Dimarcello, W. A. Reed, and P. Wisk, "Tunable dispersion compensators utilizing higher order mode fibers," *IEEE Photon. Technol. Lett.*, vol. 15, pp. 727-729, 2003
- [34] Iida, M.; Asakura, H, "A computer controlled narrow bandpass optical tunable filter using a Fourier diffraction grating in the range of 1.3-1.55  $\mu\text{m}$ ", *Journal of Lightwave Technology*, Volume: 13 , pp. 2343 - 2348 , 12 , Dec. 1995
- [35] S. Johansson, "Transport Network Involving a reconfigurable WDM network layer-A European demonstration," *Journal of Lightwave Technolgy*, vol. 14, pp. 1341-1348, 1996
- [36] M. Saleh, and M. S. Goodman, "MONET: Multiwavelength optical networking," *Journal of Lightwave Technolgy*, vol. 14, pp. 1349-1355, 1996.

- [37] *ANSYS Release 8.0 Documentation-ANSYS Element Reference*, Ansys Inc., 2004
- [38] P. H. Lissberger, A. K. Roy, and D. J. McCartney, "Narrow-band position-tuned multilayer interference filter for use in single-mode-fiber systems," *Electronic Letter*, vol. 21, pp. 798-799, Aug. 1985
- [39] *Low-Cost E Series Multifunction DAQ*, National Instruments, Austin, Tx, 2000
- [40] *3-Channel Piezo Driver – PCD-001*, General Photonics Co., Chino, CA, 2003

# Appendix A

## Drawings of Mechanical Design

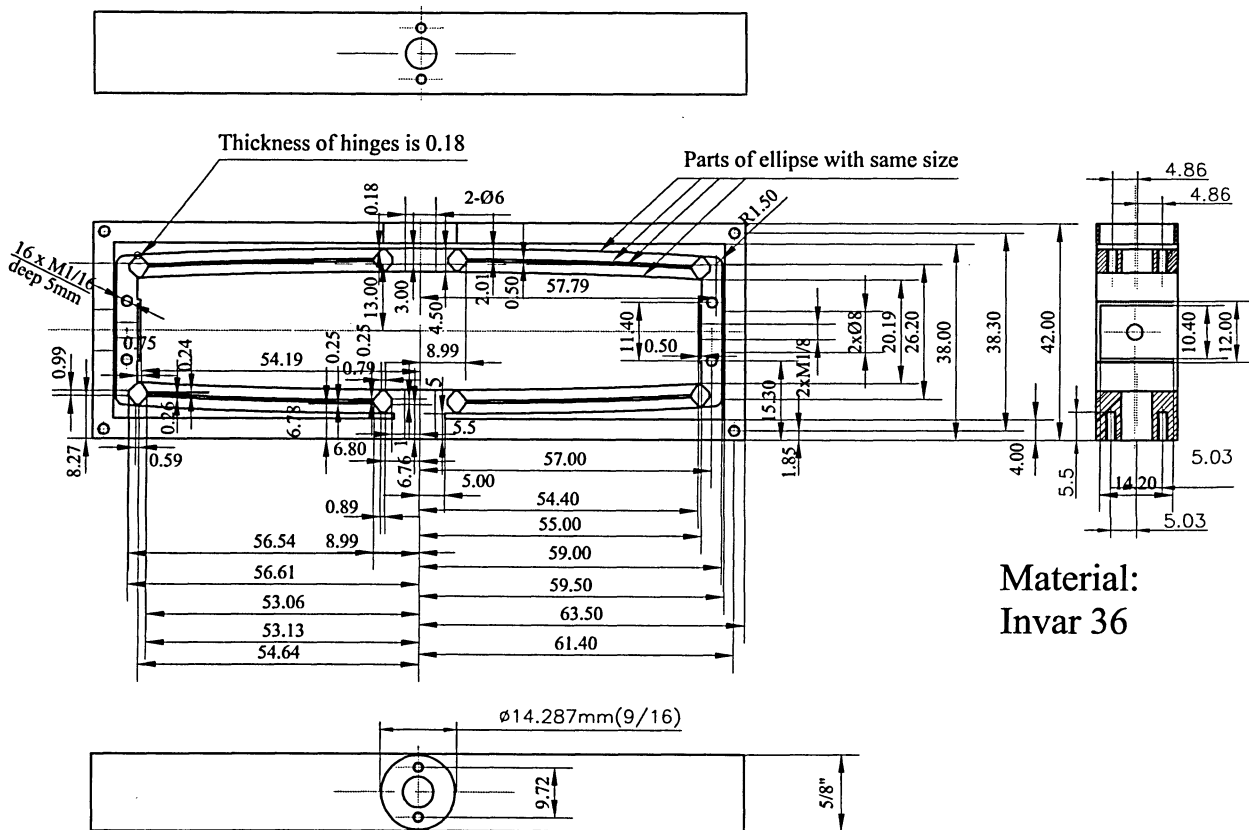
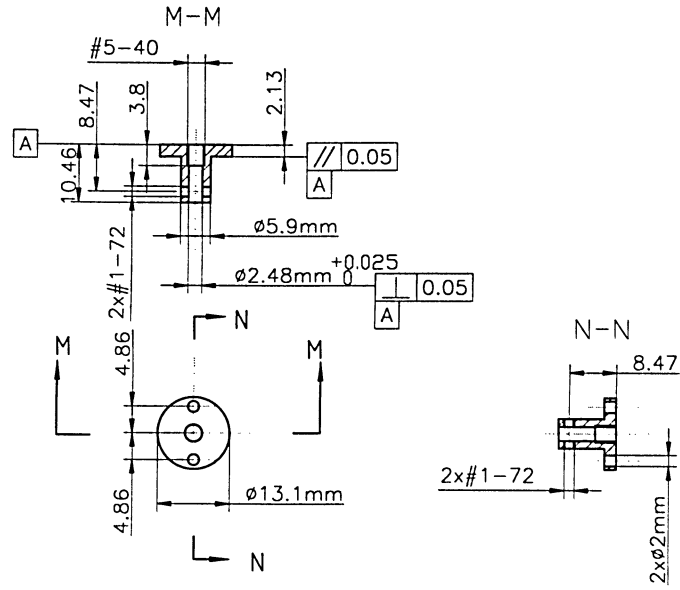
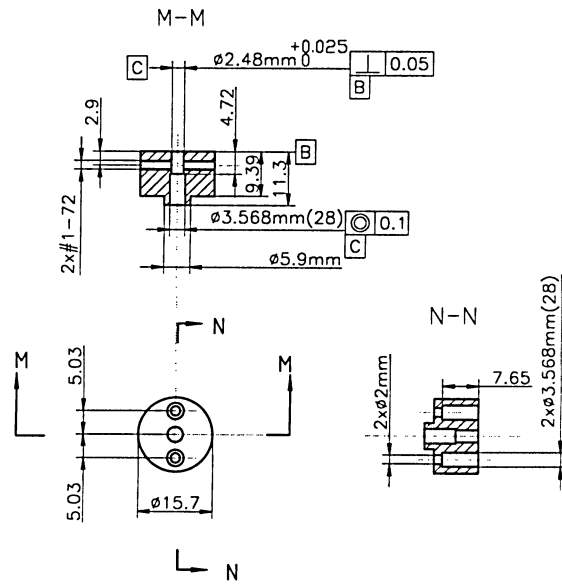


Figure A.1: Actuator



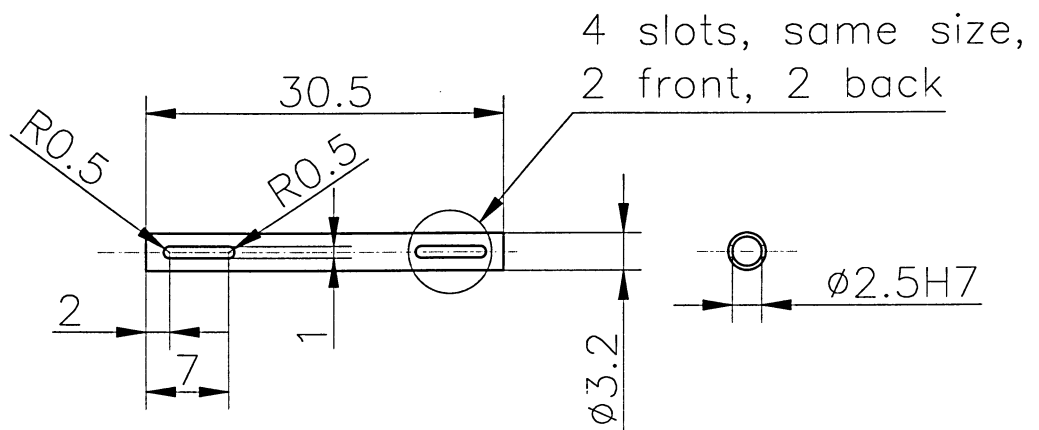
Material: Type 304 Stainless Steel

**Figure A.2: Upper Holder**



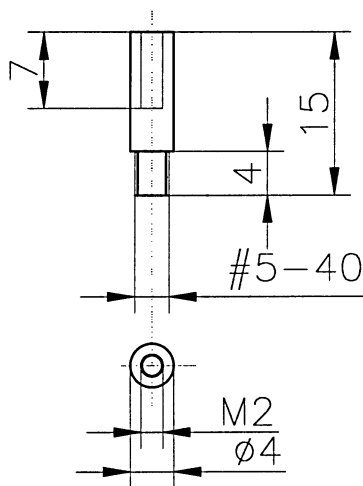
Material: Type 304 Stainless Steel

**Figure A.3: Lower Holder**



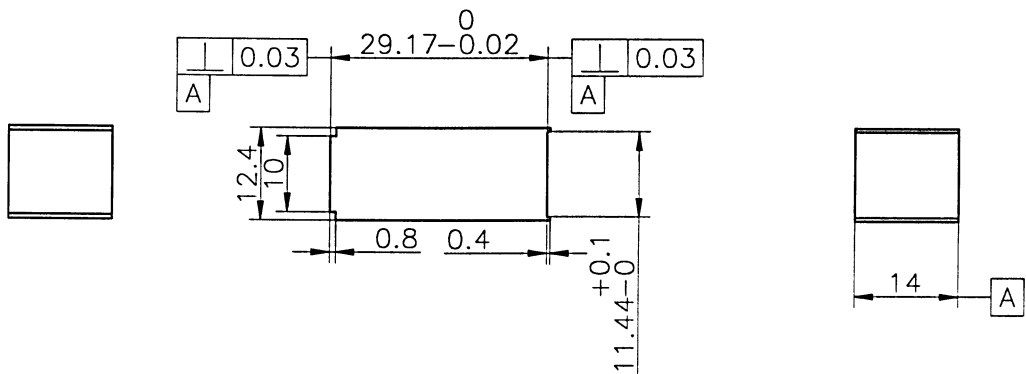
Material: Invar36

**Figure A.4: Sleeve**



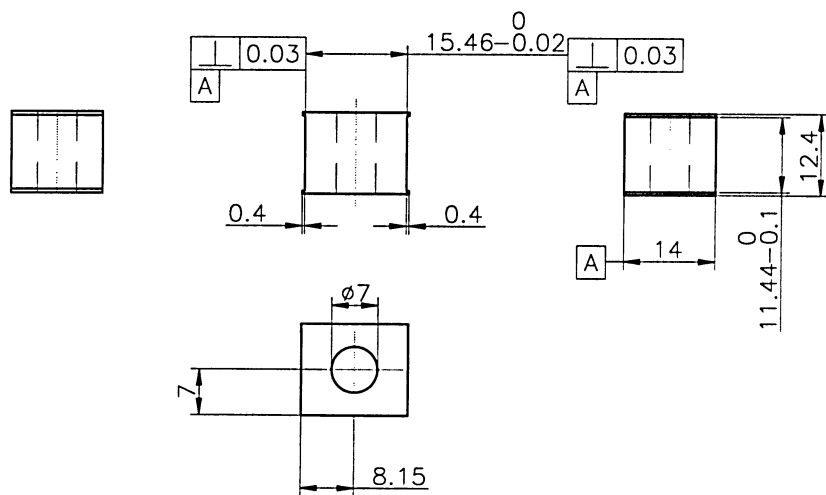
Material: #304 Stainless Steel

**Figure A.5: LVDT Holder**



Material: Invar 36

**Figure A.6: Spacer A**



Material: Type304 Stainless Steel

**Figure A.7: Spacer B**

## Appendix B

### Drawings of PCB

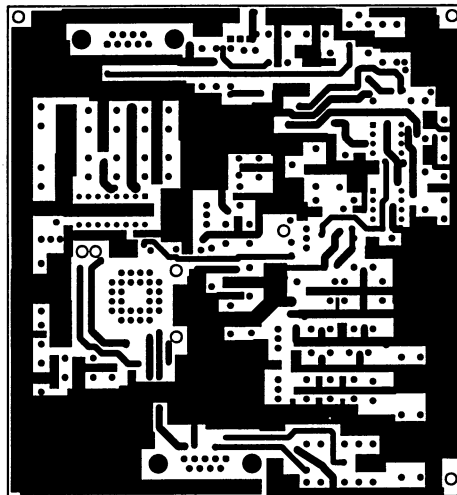


Figure B.1: Top Layer



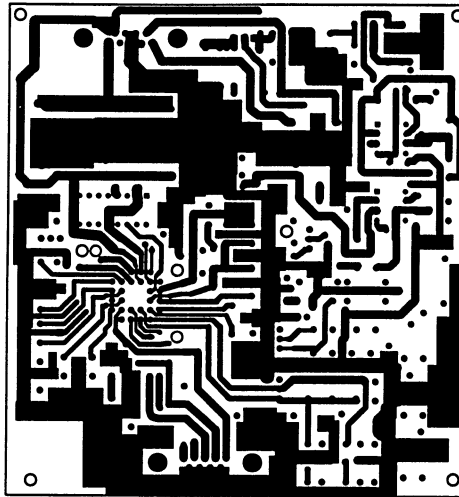


Figure B.2: Bottom Layer

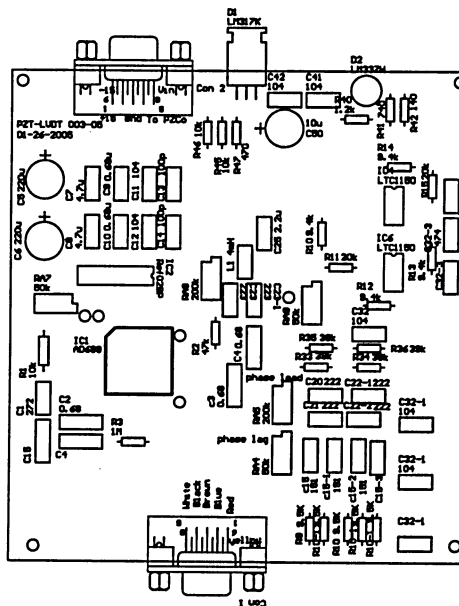
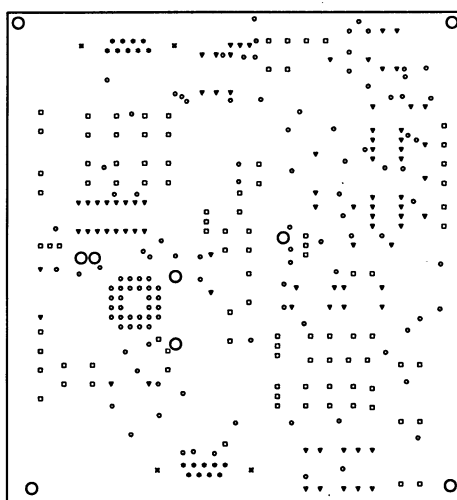


Figure B.3: Top-Over Layer



**Figure B.4: Drill**

## **Appendix C**

### **Ansys Command Log**

```

/BATCH
/COM,ANSYS RELEASE 8.0  UP20030930  12:45:07  05/10/2005
/DIST,1,1.08222638492,1
/REP,FAST
/DIST,1,1.08222638492,1
/REP,FAST
/DIST,1,0.924021086472,1
/REP,FAST
/VIEW,1,1,2,3
/ANG,1
/REP,FAST
FLIST, ALL
FKLIS, ALL
/PREP7
!*
/PNUM,KP,1
/PNUM,LINE,0
/PNUM,AREA,0
/PNUM,VOLU,0
/PNUM,NODE,0
/PNUM,TABN,0
/PNUM,SVAL,0
/NUMBER,0
!*
/PNUM,ELEM,0
/REPLOT
!*
/DIST,1,0.924021086472,1
/REP,FAST
/DIST,1,0.924021086472,1
/REP,FAST
/DIST,1,0.924021086472,1
/REP,FAST
/DIST,1,0.924021086472,1
/REP,FAST
/DIST,1,0.924021086472,1
/REP,FAST
/DIST,1,0.924021086472,1
/REP,FAST
/DIST,1,1.08222638492,1
/REP,FAST
/DIST,1,1.08222638492,1
/REP,FAST
/DIST,1,1.08222638492,1
/REP,FAST
/DIST,1,1.08222638492,1
/REP,FAST
KPLOT
/DIST,1,0.924021086472,1
/REP,FAST
/DIST,1,1.08222638492,1
/REP,FAST
GPLOT
KPLOT
LPLOT
/FOC,1,-0.3,,,1
/REP,FAST
/FOC,1,-0.3,,,1
/REP,FAST
/FOC,1,-0.3,,,1
/REP,FAST

```



```

/DIST,1,1.08222638492,1
/REP,FAST
/FOC,1,0.3,,,1
/REP,FAST
/FOC,1,0.3,,,1
/REP,FAST
/FOC,1,0.3,,,1
/REP,FAST
/FOC,1,0.3,,,1
/REP,FAST
/DIST,1,1.08222638492,1
/REP,FAST
/DIST,1,1.08222638492,1
/REP,FAST
/DIST,1,1.08222638492,1
/REP,FAST
/FOC,1,-0.3,,,1
/REP,FAST
/DIST,1,0.924021086472,1
/REP,FAST
/DIST,1,0.924021086472,1
/REP,FAST
/DIST,1,0.924021086472,1
/REP,FAST
/DIST,1,0.924021086472,1
/REP,FAST
/DIST,1,0.924021086472,1
/REP,FAST
VCLEAR, 2
/DIST,1,1.08222638492,1
/REP,FAST
/DIST,1,0.924021086472,1
/REP,FAST
/DIST,1,0.924021086472,1
/REP,FAST
/DIST,1,0.924021086472,1
/REP,FAST
/RELOT,RESIZE
/UI,MESH,OFF
SAVE,0510-thermal,db,D:\lab\pizeo\
FINISH
! /EXIT,NOSAV
/BATCH
/COM,ANSYS RELEASE 8.0 UP20030930 10:51:00 06/06/2005
RESUME,'12-17-thermal304-8.64mmhole','db',''
/COM,ANSYS RELEASE 8.0 UP20030930 10:51:02 06/06/2005
/RELOT,RESIZE
/RELOT,RESIZE
/RELOT,RESIZE
/REP7
FINISH
/CLEAR,START
/COM,ANSYS RELEASE 8.0 UP20030930 10:55:21 06/06/2005
/input,start80,ans,'C:\Program Files\Ansys Inc\v80\ANSYS\lapdl',,,,,,,,,,1
!*
/RELOT,RESIZE
RESUME,'12-17-thermal304-8.64mmhole','db',''
/COM,ANSYS RELEASE 8.0 UP20030930 10:56:03 06/06/2005
/SOLU
FLST,2,4,6,ORDE,3
FITEM,2,1

```

```

FITEM,2,-3
FITEM,2,6
!*
BFV,P51X,TEMP,10
/STATUS,SOLU
SOLVE
FINISH
/POST1
SET,FIRST
AVPRIN,0, ,
!*
PRNSOL,U,Y
AVPRIN,0, ,
!*
PRNSOL,U,Y
FINISH
/PREP7
!*
MPTEMP,,,,,,,,
MPTEMP,1,0
UIMP,1,REFT,,,0
MPDE,ALPX,1
MPDATA,ALPX,1,,0.96E-006
MPTEMP,,,,,,,,
MPTEMP,1,0
UIMP,3,REFT,,,0
MPDE,ALPX,3
MPDATA,ALPX,3,,1.71E-005
MPTEMP,,,,,,,,
MPTEMP,1,0
UIMP,4,REFT,,,0
MPDE,ALPX,4
MPDATA,ALPX,4,, -4.43E-006
FINISH
/SOL
/STATUS,SOLU
SOLVE
FINISH
/POST1
SET,FIRST
AVPRIN,0, ,
!*
PRNSOL,U,Y
/VIEW,1,1,2,3
/ANG,1
/REP,FAST
/VIEW,1,,,1
/ANG,1
/REP,FAST
/EFACE,1
AVPRIN,0, ,
!*
PLNSOL,U,Y,0,1
/DIST,1,0.924021086472,1
/REP,FAST
/DIST,1,0.924021086472,1
/REP,FAST
/DIST,1,0.924021086472,1
/REP,FAST
/DIST,1,0.924021086472,1
/REP,FAST

```

```

/DIST,1,1.08222638492,1
/REP,FAST
/DIST,1,1.08222638492,1
/REP,FAST
/DIST,1,1.08222638492,1
/REP,FAST
/DIST,1,1.08222638492,1
/REP,FAST
/DIST,1,1.08222638492,1
/REP,FAST
/DIST,1,1.08222638492,1
/REP,FAST
/DIST,1,0.924021086472,1
/REP,FAST
/DIST,1,0.924021086472,1
/REP,FAST
/DIST,1,0.924021086472,1
/REP,FAST
/DIST,1,0.924021086472,1
/REP,FAST
/DIST,1,0.924021086472,1
/REP,FAST
/DIST,1,0.924021086472,1
/REP,FAST
/DIST,1,1.08222638492,1
/REP,FAST
/DIST,1,1.08222638492,1
/REP,FAST
FINISH
/PREP7
!*
MPTEMP,,,,,,,,
MPTEMP,1,0
UIMP,4,REFT,,,0
MPDE,ALPX,4
MPDATA,ALPX,4,,-4.4E-006
MPTEMP,,,,,,,,
MPTEMP,1,0
UIMP,3,REFT,,,0
MPDE,ALPX,3
MPDATA,ALPX,3,,1.73E-005
FINISH
/SOL
/STATUS,SOLU
SOLVE
FINISH
/POST1
SET,FIRST
/EFACE,1
AVPRIN,0, ,
!*
PLNSOL,U,Y,0,1
AVPRIN,0, ,
!*
PRNSOL,U,Y
SAVE,0606-1,db,D:\lab\pizeo\
FINISH
! /EXIT,NOSAV
/BATCH

```



```

/COM,ANSYS RELEASE 8.0  UP20030930  11:22:50  06/10/2005
RESUME,'12-17-thermal304-8.64mmhole','db',''
/COM,ANSYS RELEASE 8.0  UP20030930  11:22:51  06/10/2005
/PREP7
!*
MPTEMP,,,,,,,,
MPTEMP,1,0
UIMP,1,REFT,,,0
MPDE,ALPX,1
MPDATA,ALPX,1,,0.9E-006
MPTEMP,,,,,,,,
MPTEMP,1,0
UIMP,3,REFT,,,0
MPDE,ALPX,3
MPDATA,ALPX,3,,1.69E-005
MPTEMP,,,,,,,,
MPTEMP,1,0
UIMP,4,REFT,,,0
MPDE,ALPX,4
MPDATA,ALPX,4,, -5.1E-006
FKLIS, ALL
FINISH
/SOL
FLST,2,4,6,ORDE,3
FITEM,2,1
FITEM,2,-3
FITEM,2,6
!*
BFV,P51X,TEMP,10
/STATUS,SOLU
SOLVE
FINISH
/POST1
SET,FIRST
/EFACE,1
AVPRIN,0, ,
!*
PLNSOL,U,Y,0,1
/VIEW,1,,,1
/ANG,1
/REP,FAST
/DIST,1,1.08222638492,1
/REP,FAST
AVPRIN,0, ,
!*
PRNSOL,U,Y
FINISH
/PREP7
!*
MPTEMP,,,,,,,,
MPTEMP,1,0
UIMP,1,REFT,,,0
MPDE,ALPX,1
MPDATA,ALPX,1,,9.6E-007
FINISH
/SOL
/STATUS,SOLU
SOLVE
FINISH
/POST1
SET,FIRST

```

```

/EFACE,1
AVPRIN,0, ,
!*
PLNSOL,U,Y,0,1
FINISH
/PREP7
!*
MPTEMP,,,,,,,,
MPTEMP,1,0
UIMP,1,REFT,,,0
MPDE,ALPX,1
MPDATA,ALPX,1,,9E-007
MPTEMP,,,,,,,,
MPTEMP,1,0
UIMP,3,REFT,,,0
MPDE,ALPX,3
MPDATA,ALPX,3,,1.73E-005
FINISH
/SOL
/STATUS,SOLU
SOLVE
FINISH
/POST1
SET,FIRST
/EFACE,1
AVPRIN,0, ,
!*
PLNSOL,U,Y,0,1
FINISH
/FILNAME,0606-1,1
/BATCH
/COM,ANSYS RELEASE 8.0  UP20030930      14:46:10  06/10/2005
RESUME,'12-17-thermal304-8.64mmhole','db',','
/COM,ANSYS RELEASE 8.0  UP20030930      14:46:12  06/10/2005
/REPLOT,RESIZE
/PREP7
!*
MPTEMP,,,,,,,,
MPTEMP,1,0
UIMP,1,REFT,,,0
MPDE,ALPX,1
MPDATA,ALPX,1,,0.9E-006
MPTEMP,,,,,,,,
MPTEMP,1,0
MPDE,NUXY,1
MPDE,NUYZ,1
MPDE,NUXZ,1
MPDE,PRXY,1
MPDE,PRYZ,1
MPDE,PRXZ,1
MPDE,EX,1
MPDATA,EX,1,,1.41E+011
MPDE,EY,1
MPDATA,EY,1,,1.41E+011
MPDE,EZ,1
MPDATA,EZ,1,,1.41E+011
MPDATA,PRXY,1,,0.29
MPDATA,PRYZ,1,,0.29
MPDATA,PRXZ,1,,0.29
MPDE,GXY,1
MPDATA,GXY,1,,5.78E+010

```

```

MPDE,GYZ,1
MPDATA,GYZ,1,,5.78E+010
MPDE,GXZ,1
MPDATA,GXZ,1,,5.78E+010
MPTEMP,,,,,,,,
MPTEMP,1,0
UIMP,3,REFT,,,0
MPDE,ALPX,3
MPDATA,ALPX,3,,1.7E-005
MPTEMP,,,,,,,,
MPTEMP,1,0
UIMP,4,REFT,,,0
MPDE,ALPX,4
MPDATA,ALPX,4,,-6.3E-006
FINISH
/SOL
FLST,2,4,6,ORDE,3
FITEM,2,1
FITEM,2,-3
FITEM,2,6
!*
BFV,P51X,TEMP,10
FINISH
/POST1
FINISH
/SOL
/STATUS,SOLU
SOLVE
/VIEW,1,,,1
/ANG,1
/REP,FAST
/DIST,1,1.08222638492,1
/REP,FAST
/DIST,1,1.08222638492,1
/REP,FAST
/DIST,1,1.08222638492,1
/REP,FAST
FINISH
/POST1
SET,FIRST
FKLIS, ALL
SET,FIRST
DALIS, ALL
/EFACE,1
AVPRIN,0, ,
!*
PLNSOL,U,Y,0,1
AVPRIN,0, ,
!*
PRNSOL,DOF,
FINISH
/PREP7
!*
MPTEMP,,,,,,,,
MPTEMP,1,0
UIMP,1,REFT,,,0
MPDE,ALPX,1
MPDATA,ALPX,1,,9E-007
/PNUM,KP,0
/PNUM,LINE,0
/PNUM,AREA,0

```

```

/PNUM,VOLU,0
/PNUM,NODE,1
/PNUM,TABN,0
/PNUM,SVAL,0
/NUMBER,0
!*
/PNUM,ELEM,0
/REPLOT
!*
/FOC,1,0.3,,,1
/REP,FAST
/FOC,1,0.3,,,1
/REP,FAST
/DIST,1,0.924021086472,1
/REP,FAST
/DIST,1,0.924021086472,1
/REP,FAST
/DIST,1,0.924021086472,1
/REP,FAST
/DIST,1,0.924021086472,1
/REP,FAST
/DIST,1,0.924021086472,1
/REP,FAST
/DIST,1,0.924021086472,1
/REP,FAST
/DIST,1,0.924021086472,1
/REP,FAST
/DIST,1,0.924021086472,1
/REP,FAST
/DIST,1,0.924021086472,1
/REP,FAST
/DIST,1,0.924021086472,1
/REP,FAST
/DIST,1,0.924021086472,1
/REP,FAST
/DIST,1,0.924021086472,1
/REP,FAST
/DIST,1,0.924021086472,1
/REP,FAST
/DIST,1,0.924021086472,1
/REP,FAST
/DIST,1,0.924021086472,1
/REP,FAST
/DIST,1,1.08222638492,1
/REP,FAST
FINISH
/SOL
FINISH
/POST1
AVPRIN,0, ,
!*
PRNSOL,DOF,
klist,all,,,coord
FINISH
/REP7
FINISH
/SOL
FLST,2,4,6,ORDE,3
FITEM,2,1

```

```

FITEM,2,-3
FITEM,2,6
/DIST,1,1.08222638492,1
/REP,FAST
/DIST,1,1.08222638492,1
/REP,FAST
/DIST,1,1.08222638492,1
/REP,FAST
/DIST,1,1.08222638492,1
/REP,FAST
/DIST,1,1.08222638492,1
/REP,FAST
/DIST,1,1.08222638492,1
/REP,FAST
/DIST,1,1.08222638492,1
/REP,FAST
/DIST,1,1.08222638492,1
/REP,FAST
/FOC,1,-0.3,,,1
/REP,FAST
/FOC,1,-0.3,,,1
/REP,FAST
/FOC,1,-0.3,,,1
/REP,FAST
/DIST,1,1.08222638492,1
/REP,FAST
/DIST,1,1.08222638492,1
/REP,FAST
/DIST,1,1.08222638492,1
/REP,FAST
/DIST,1,0.924021086472,1
/REP,FAST
/PNUM,KP,0
/PNUM,LINE,0
/PNUM,AREA,0
/PNUM,VOLU,0
/PNUM,NODE,0
/PNUM,TABN,0
/PNUM,SVAL,0
/NUMBER,0
!*
/PNUM,ELEM,0
/REPLOT
!*
SAVE,0610-4,db,C:\PROGRA~1\ANSYSI~1\v80\ANSYS\bin\intel\
/DIST,1,1.08222638492,1
/REP,FAST
FINISH
/REP7
VCLEAR, 1
VDELE, 1,,1
FINISH
/SOL
/STATUS,SOLU
SOLVE
/PNUM,KP,0
/PNUM,LINE,0
/PNUM,AREA,0
/PNUM,VOLU,0
/PNUM,NODE,1
/PNUM,TABN,0

```

```

/PNUM,SVAL,0
/NUMBER,0
!*
/PNUM,ELEM,0
/REPLOT
!*
FINISH
/POST1
SET,FIRST
/EFACE,1
AVPRIN,0, ,
!*
PLNSOL,U,X,0,1
/DIST,1,1.08222638492,1
/REP,FAST
/DIST,1,1.08222638492,1
/REP,FAST
/FOC,1,0.3,,1
/REP,FAST
/FOC,1,0.3,,1
/REP,FAST
/DIST,1,0.924021086472,1
/REP,FAST
/DIST,1,0.924021086472,1
/REP,FAST
/DIST,1,0.924021086472,1
/REP,FAST
/DIST,1,0.924021086472,1
/REP,FAST
/DIST,1,0.924021086472,1
/REP,FAST
/DIST,1,0.924021086472,1
/REP,FAST
/DIST,1,0.924021086472,1
/REP,FAST
/DIST,1,0.924021086472,1
/REP,FAST
/DIST,1,0.924021086472,1
/REP,FAST
/DIST,1,0.924021086472,1
/REP,FAST
/DIST,1,0.924021086472,1
/REP,FAST
/DIST,1,1.08222638492,1
/REP,FAST
/DIST,1,1.08222638492,1
/REP,FAST
/DIST,1,1.08222638492,1
/REP,FAST
/DIST,1,1.08222638492,1
/REP,FAST
/DIST,1,0.924021086472,1
/REP,FAST
/DIST,1,0.924021086472,1
/REP,FAST
/DIST,1,0.924021086472,1
/REP,FAST
/DIST,1,0.924021086472,1
/REP,FAST

```



```

MPDE,EX,4
MPDATA,EX,4,,8E+011
MPDE,EY,4
MPDATA,EY,4,,8E+011
MPDE,EZ,4
MPDATA,EZ,4,,8E+011
MPDATA,PRXY,4,,0.3
MPDATA,PRYZ,4,,0.3
MPDATA,PRXZ,4,,0.3
MPDE,GXY,4
MPDATA,GXY,4,,8E+010
MPDE,GYZ,4
MPDATA,GYZ,4,,8E+010
MPDE,GXZ,4
MPDATA,GXZ,4,,8E+010
MPTEMP,,,,,,,,
MPTEMP,1,0
MPDE,NUXY,3
MPDE,NUYZ,3
MPDE,NUXZ,3
MPDE,PRXY,3
MPDE,PRYZ,3
MPDE,PRXZ,3
MPDE,EX,3
MPDATA,EX,3,,2E+011
MPDE,EY,3
MPDATA,EY,3,,2E+011
MPDE,EZ,3
MPDATA,EZ,3,,2E+011
MPDATA,PRXY,3,,0.29
MPDATA,PRYZ,3,,0.29
MPDATA,PRXZ,3,,0.29
MPDE,GXY,3
MPDATA,GXY,3,,8.6E+010
MPDE,GYZ,3
MPDATA,GYZ,3,,8.6E+010
MPDE,GXZ,3
MPDATA,GXZ,3,,8.6E+010
FINISH
/SOL
FLST,2,4,3,ORDE,3
FITEM,2,63
FITEM,2,98
FITEM,2,-100
!*
/GO
FK,P51X,FX,-10
FLST,2,3,6,ORDE,3
FITEM,2,2
FITEM,2,-3
FITEM,2,6
!*
BFV,P51X,TEMP,10
FINISH
/POST1
FINISH
/SOL
/STATUS,SOLU
SOLVE
DALIS, ALL
FINISH

```



```

/POST1
SET,FIRST
AVPRIN,0, ,
!*
PRNSOL,DOF,
/ANG,1,-30,XS,1
/REP,FAST
/ANG,1,-30,YS,1
/REP,FAST
/ANG,1,-30,YS,1
/REP,FAST
/ANG,1,30,XS,1
/REP,FAST
/ANG,1,-30,XS,1
/REP,FAST
/ANG,1,30,YS,1
/REP,FAST
/DIST,1,1.08222638492,1
/REP,FAST
/DIST,1,1.08222638492,1
/REP,FAST
/DIST,1,1.08222638492,1
/REP,FAST
/DIST,1,1.08222638492,1
/REP,FAST
/DIST,1,0.924021086472,1
/REP,FAST
/DIST,1,0.924021086472,1
/REP,FAST
FINISH
/SOL
SAVE,t,db,C:\PROGRA~1\ANSYSI~1\v80\ANSYS\bin\intel\
FINISH
! /EXIT

```